LITHOS 416-417 (2022) 106643

Contents lists available at ScienceDirect

LITHOS

journal homepage: www.elsevier.com/locate/lithos

CO_2 storage in the Antarctica Sub-Continental Lithospheric Mantle as revealed by intra- and inter-granular fluids

Federico Casetta [a,*], Andrea L. Rizzo [b,c,d], Barbara Faccini [c], Theodoros Ntaflos [a], Rainer Abart [a], Gabriele Lanzafame [e], Luca Faccincani [c], Lucia Mancini [f,g], Pier Paolo Giacomoni [c], Massimo Coltorti [b,c]

[a] Department of Lithospheric Research, University of Vienna, Althanstraße 14, 1090 Vienna, Austria
[b] Istituto Nazionale di Geofisica e Vulcanologia, Sezione di Palermo, Via Ugo La Malfa 153, 90146 Palermo, Italy
[c] Department of Physics and Earth Sciences, University of Ferrara, Via Saragat 1, 44121 Ferrara, Italy
[d] Istituto Nazionale di Geofisica e Vulcanologia, Sezione di Milano, Via Alfonso Corti 12, 20133 Milano, Italy
[e] Department of Biological, Geological and Environmental Sciences, University of Catania, Catania, Italy
[f] Elettra-Sincrotrone Trieste S.C.p.A, SS 14 – km 153,5 in Area Science Park, 34149 Basovizza, Trieste, Italy
[g] LINXS – Lund Institute for advanced Neutron and X-ray Science, Scheelevägen 19, 223 70 Lund, Sweden

ARTICLE INFO

Keywords:
CO_2 storage
Sub-Continental Lithospheric Mantle
Alkaline metasomatism
Fluid inclusions
Synchrotron X-ray microtomography
Inter-granular fluids

ABSTRACT

The investigation of the role played by CO_2 circulating within the mantle during partial melting and metasomatic/refertilization processes, together with a re-consideration of its storage capability and re-cycling in the lithospheric mantle, is crucial to unravel the Earth's main geodynamic processes. In this study, the combination of petrology, CO_2 content trapped in bulk rock- and mineral-hosted fluid inclusions (FI), and 3D textural and volumetric characterization of intra- and inter-granular microstructures was used to investigate the extent and modality of CO_2 storage in depleted and fertile (or refertilized) Sub-Continental Lithospheric Mantle (SCLM) beneath northern Victoria Land (NVL, Antarctica). Prior to xenoliths entrainment by the host basalt, the Antarctic SCLM may have stored 0.2 vol% melt and 1.1 vol% fluids, mostly as FI trails inside mineral phases but also as inter-granular fluids. The amount of CO_2 stored in FI varies from 0.1 $\mu g_{(CO2)}/g_{(sample)}$ in olivine from the anhydrous mantle xenoliths at Greene Point and Handler Ridge, up to 187.3 μg/g in orthopyroxene from the highly metasomatized amphibole-bearing lherzolites at Baker Rocks, while the corresponding bulk CO_2 contents range from 0.3 to 57.2 μg/g.

Irrespective of the lithology, CO_2 partitioning is favoured in orthopyroxene and clinopyroxene-hosted FI (olivine: orthopyroxene = 0.10 ± 0.06 to 0.26 ± 0.09; olivine: clinopyroxene = 0.10 ± 0.05 to 0.27 ± 0.14). The $H_2O/(H_2O + CO_2)$ molar ratios obtained by comparing the CO_2 contents of FI to the H_2O amount retained in pyroxene lattices vary between 0.72 ± 0.17 and 0.97 ± 0.03, which is well comparable with the values measured in olivine-hosted melt inclusions from Antarctic primary lavas and assumed as representative of the partition of volatiles at the local mantle conditions. From the relationships between mineral chemistry, thermo-, oxybarometric results and CO_2 contents in mantle xenoliths, we speculate that relicts of CO_2-depleted mantle are present at Greene Point, representing memory of a CO_2-poor tholeiitic refertilization related to the development of the Jurassic Ferrar large magmatic event. On the other hand, a massive mobilization of CO_2 took place before the (melt-related) formation of amphibole veins during the alkaline metasomatic event associated with the Cenozoic rift-related magmatism, in response to the storage and recycling of CO_2-bearing materials into the Antarctica mantle likely induced by the prolonged Ross subduction.

1. Introduction

Along with being a major constituent of the atmosphere and the hydrosphere, carbon acts as a catalyst for the main processes taking place in the asthenosphere-lithosphere system and is one of the main regulators for the habitability of our planet. The deep C cycling between

* Corresponding author.
E-mail address: federico.casetta@univie.ac.at (F. Casetta).

https://doi.org/10.1016/j.lithos.2022.106643
Received 26 July 2021; Received in revised form 25 January 2022; Accepted 22 February 2022
Available online 1 March 2022

mantle and surface, due to the long-term combination of subduction, metasomatism/refertilization processes, volatiles fluxing, and emission through volcanism, exerts a key control on both climate and geodynamics. As a consequence, understanding the C cycle in the Earth's deepest reservoirs, which may contain >90% of the terrestrial carbon (Dasgupta, 2013; Dasgupta and Hirschmann, 2010; Foley and Fischer, 2017; Hazen and Schiffries, 2013; Suarez et al., 2019), is crucial for modelling the evolution of our planet and understanding climate changes (Howell et al., 2020; Malusà et al., 2018; Plank and Manning, 2019;).

Because of its prolonged record of melt extraction and metasomatism/refertilization processes acting over different timescales, the Sub-Continental Lithospheric Mantle (SCLM) can provide important insights into how and where volatiles are stored and/or migrate through the deep Earth. In the lithospheric mantle, C, O, H, S and halogens can be incorporated into accessory phases, nominally anhydrous minerals (NAMs) or fluid/melt phases (Andersen and Neumann, 2001; Frezzotti and Touret, 2014; Roedder, 1965; Thompson, 1992) and exert a key control on mantle rheological properties, melting/enrichment processes and magma genesis (Dasgupta et al., 2007; Dasgupta and Hirschmann, 2006; Taylor and Green, 1988; Wallace and Green, 1991; Wyllie, 1978). Thanks to the advancements in both analytical and high-resolution X-ray imaging techniques, the study of inter- and intra-granular fluid/glass phases in mantle xenoliths may clarify the relationships between volatiles/melts migration in the SCLM and the onset of metasomatic/refertilization events and magma genesis (Créon et al., 2017; Franz and Wirth, 1997; Frezzotti et al., 2002, 2010; Zhu et al., 2011).

In northern Victoria Land (NVL, Antarctica), various suites of modally and chemically variable ultramafic xenoliths were brought to the surface by the Cenozoic magmatism associated with the development of the West Antarctic Rift System (WARS). The xenoliths, found at Greene Point, Baker Rocks and Handler Ridge (Fig. 1), record a long-lasting series of refertilization/metasomatic processes that took place after melt extraction (Coltorti et al., 2021). They are thus perfect candidates for tracking the evolution of portions of the SCLM during multiple geodynamic events. Indeed, the NVL lithospheric mantle bears witness of moderate to strong depletion event/s with ages as old as Archean (Melchiorre et al., 2011). During the Phanerozoic, it was affected by: i) the long-lasting (550–110 *Ma*) subduction of oceanic lithosphere along the Paleo-Pacific margin of Gondwana, intimately linked to the Ross Orogeny (Kleinschmidt et al., 1987; Mukasa and Dalziel, 2000); ii) the Jurassic magmatism of the Ferrar Large Igneous Province (185–180 *Ma*; Elliot and Fleming, 2018); iii) the Late Cretaceous rifting phase that led to the formation of the WARS; iv) the Cenozoic alkaline magmatism associated with rift maturation (Giacomoni et al., 2020; Panter et al., 2018). In the last years, various studies focused on the distribution of noble gases and halogens in fluid inclusions (FI) and showed that the volatiles retained in NVL ultramafic xenoliths bear witness of interactions between a depleted mantle and subduction-related fluids (Broadley et al., 2016; Correale et al., 2019: Day et al., 2019). Besides ruling out the existence of a mantle plume beneath this area, these results highlighted that the volatiles trapped in the local SCLM are able to preserve the memory of old geodynamic events (namely, the 550 to 110 *Ma* subduction of oceanic lithosphere). However, the scarce information about the amount and mode of CO_2 storage in the mantle beneath Antarctica makes it difficult to fully understand how deep carbon was mobilized from the mantle during continental rifting (e.g., Muirhead et al., 2020), and apprehend how the long-term recycling of CO_2 is related to the complex geodynamic evolution of the area.

We present a petrological study of ultramafic xenoliths from NVL, which was combined with measurements of CO_2 released from bulk-rock- and mineral-hosted FI, and 3D textural and volumetric characterization of intra- and inter-granular microstructures, in order to investigate how and where CO_2 is stored in depleted and fertile (or refertilized) mantle portions. Beyond exploring the role played by intra- and inter-granular fluids circulating during melt extraction and/or enrichment episodes, our results allowed to assess the mobility of CO_2 during the complex geodynamic evolution experienced by the Antarctica SCLM. To a broader scale, this multidisciplinary approach contributes to our understanding of the role played by C during magma genesis and metasomatism/refertilization processes in the mantle.

2. Role and storage of CO_2 in the SCLM: State of the art

In a cycle driven by plate tectonics, carbon moves from the subducting oceanic (or sometimes continental) crust and the attached hydrothermalized lithospheric mantle to the deep mantle, and is partially recycled to erupting volcanoes (Dasgupta, 2013; Farsang et al., 2021; Plank and Manning, 2019). The occurrence of CO_2 in the lithospheric mantle and its relationships with local to large-scale geodynamic processes have been addressed from various sides. Experimental petrology has proven to be one of the most effective ways to explore the impact of CO_2 on petrogenesis, mineral phase stability and metasomatic modification of the mantle. Together with H_2O, CO_2 lowers the solidus of a peridotitic system, thus acting as catalyst for partial melting (e.g., Canil, 1990; Dasgupta and Hirschmann, 2006; Eggler, 1976; Taylor and Green, 1988; Wyllie, 1977, 1978). Indeed, the presence and relative activity of H_2O, CO_2 and other volatile species (e.g., fluorine) in the mantle has a strong impact on the presence and stability of easily fusible accessory phases, such as amphibole, phlogopite, and/or carbonates (Condamine and Médard, 2014; Foley, 1991; Tumiati et al., 2013). In turn, the susceptibility of these phases for partial melting leads to the generation of magmas with extremely variable (and sometimes exotic) compositions, i.e. from basaltic to highly alkaline or carbonatitic (e.g., Casetta et al., 2020, 2021; Dasgupta et al., 2007; Pilet, 2015; Wallace and Green, 1991). Again, the mobilization of C-H-O fluids and/or carbonatitic melts caused by the deep recycling of C from subducting slabs leads to the formation of diamonds in the sub-cratonic lithospheric keels (Galvez and Pubellier, 2019; Plank and Manning, 2019; Stachel and Harris, 2009).

Although a direct quantification of the amount of CO_2 (or other volatiles) currently stored in the lithospheric mantle is not possible, indirect evidence on the circulation of volatile-rich fluid/melt phases comes from the study of mantle xenoliths, diamonds, and inclusions hosted in mantle and/or magmatic minerals. However, due to the onset of CO_2 degassing at great depths, the budget of C stored in the mantle cannot be properly constrained and still remains a matter of debate (Hirschmann, 2018; Marty, 2012). To address this problem, measurements of volatiles concentration can be performed on primary melt inclusions, which represent poorly degassed melts entrapped in mineral phases early after magma segregation from the mantle. In this respect, the distribution of incompatible elements behaving similarly to C during partial melting (Nb, Ba, Cl) in olivine-hosted melt inclusions from Mid Ocean Ridge Basalts (MORB) led many authors to speculate that the Depleted MORB Mantle (DMM) can store 73–205 ppm CO_2 (Rosenthal et al., 2015; Saal et al., 2002), although local interactions with plume material may lead to a heterogeneous enrichment of the DMM, with CO_2 contents as high as 1980 ppm (Cottrell et al., 2019). On the other hand, enriched mantle domains in intraplate settings mostly contain between 600 and 2600 ppm CO_2 (Aiuppa et al., 2021; Anderson and Poland, 2017; Boudoire et al., 2018; Hauri et al., 2018; Le Voyer et al., 2017; Rosenthal et al., 2015). The counterpart of these models comes from the volatiles measured directly in mantle-derived peridotitic xenoliths - in NAMs, hydrous minerals, glasses and FI -, which often experience modal (addition of new phases), cryptic (chemical modification of the original phases), or stealth (addition of new phases mineralogically indistinguishable from the primary assemblage) metasomatism (O'Reilly and Griffin, 2013). Such reactions can be variably caused by the infiltration of tholeiitic to alkaline or carbonatitic melts, bearing large amounts of dissolved volatiles or partially coexisting with an already exsolved fluid phase, that may be trapped as inclusions in minerals (Frezzotti and

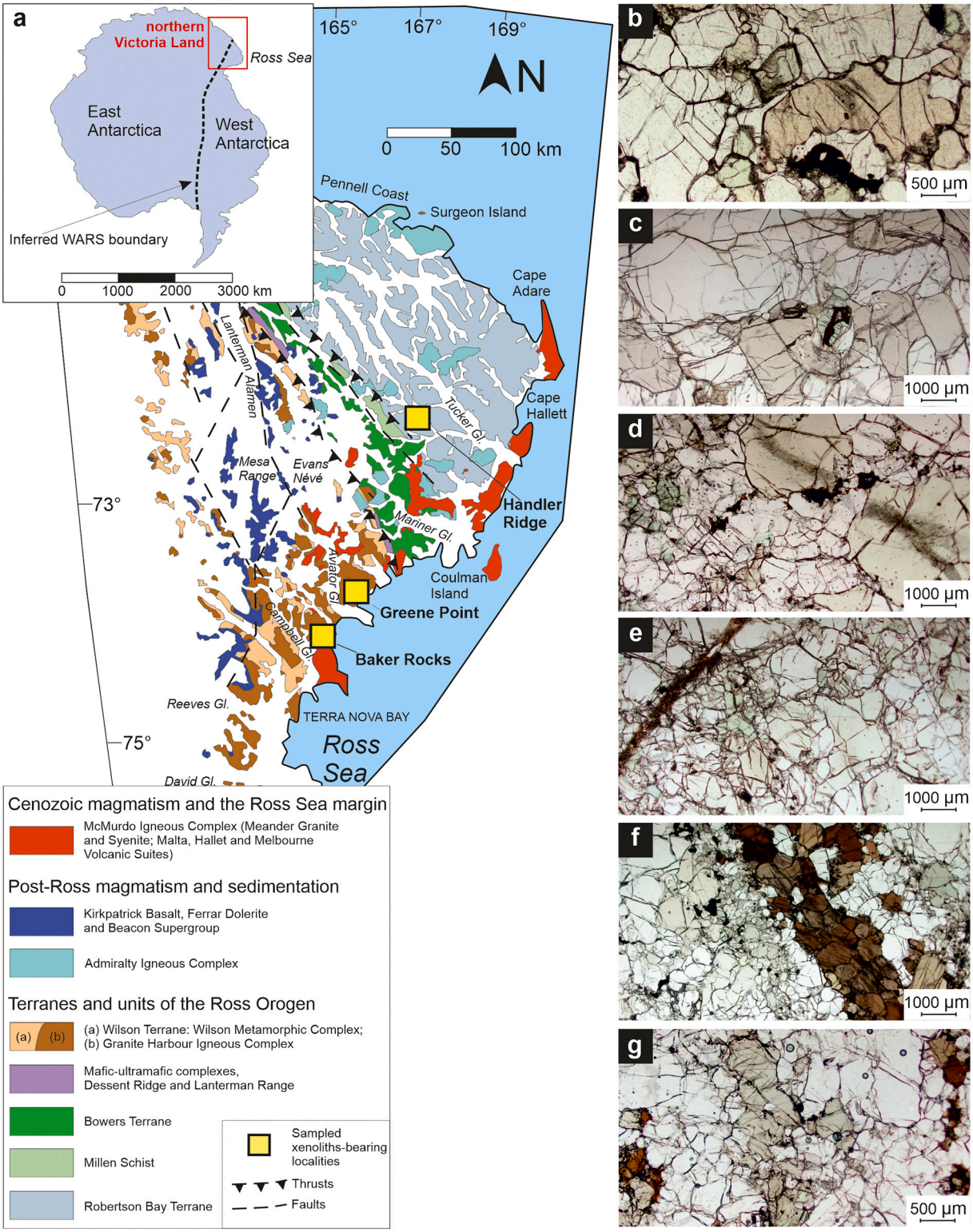

Fig. 1. (a) Simplified geological map of northern Victoria Land, modified from Coltorti et al. (2021). Squares indicate the location of the studied xenolith localities: Handler Ridge, Greene Point and Baker Rocks. On the upper left, the sketch map of Antarctica shows the location of northern Victoria Land and the inferred West Antarctic Rift System (WARS) boundary (Panter et al., 2018). Gl. = glacier. (b) Protogranular lherzolite from Handler Ridge; (c) Protogranular harzburgite from Greene Point; (d) Porphyroclastic lherzolite from Baker Rocks; (e) Porphyroclastic olivine-websterite cut by host basalt-related vein from Baker Rocks; (f) Composed sample (lherzolite + hornblendite vein) from Baker Rocks; (g) Amphibole-bearing porphyroclastic lherzolite from Baker Rocks.

Touret, 2014; Frezzotti et al., 2002, 2010; Scambelluri et al., 2009;). Undoubtedly, the behaviour of C within the SCLM is still largely unexplored, owing to its heterogeneous distribution and long-lasting recycling, that depends on the volatiles fate in subduction zones as well as on mantle convection (see Foley and Fischer, 2017; Hauri et al., 2018; Shirey et al., 2019). In this framework, the combination of FI chemistry, petrology and 3D textural/volumetric imaging on mantle xenoliths offers the possibility to achieve a detailed picture of carbon distribution in mantle phases and its cycling in the SCLM. A comparison between our results, previously published data on volatile contents in peridotite minerals, olivine-hosted melt inclusions in magmas and models on the metasomatic/refertilization affecting the Antarctic mantle (Coltorti et al., 2021) was put forward to enhance our comprehension of the role played by CO_2 during the articulated geodynamic evolution of the area.

3. Analytical methods

3.1. Sample location and preparation

Over the last couple of years, the textural and compositional features of mantle xenoliths from NVL at Greene Point, Baker Rocks and Handler Ridge (Fig. 1) were explored in detailed petrological studies (Bonadiman et al., 2009, 2014; Coltorti et al., 2004, 2021; Melchiorre et al., 2011; Pelorosso et al., 2016, 2017; Perinelli et al., 1998, 2006). For the purpose of this work, 19 samples, most representative of the three NVL xenolith suites and characterized by large dimensions (diameter $>$ 5 cm) were selected and partitioned into:

- Polished thin sections (thickness of 80 μm) for textural observations and in situ mineral chemistry analyses;
- Cylinders with diameter of ~4 mm and vertical size of ~10 mm, for 3D X-ray microtomographic imaging;
- Crushed matrices from which hundreds of milligrams of olivine, orthopyroxene, clinopyroxene and amphibole (when present) crystals were isolated by hand picking for measuring the CO_2 content in FI.

3.2. Mineral chemistry analyses

Mineral phase major element chemistry was determined by using a Cameca SXFive FE electron microprobe equipped with five WD and one ED spectrometers hosted at the Department of Lithospheric Research at the University of Vienna (Austria). The operating conditions were as follows: 15 kV accelerating voltage, 20 nA beam current, and 20 s counting time on peak position. Natural and synthetic standards were used for calibration, and PAP corrections were applied to the intensity data (Pouchou and Pichoir, 1991). Detection limits ranged from 0.01 to 0.06 wt%.

3.3. Synchrotron Radiation Computed microTomography (SR μCT), 3D image processing and analysis

Experiments aimed at identifying and quantifying the abundance of inter- and intra-granular glasses and voids in mantle xenoliths were carried out by performing high-resolution SR μCT scans in phase-contrast mode (Polacci et al., 2010) at the SYRMEP beamline of the Elettra synchrotron facility (Basovizza, Trieste, Italy). Scans were acquired in local area or region-of-interest mode (Maire and Withers, 2014), with a voxel size of 1.37 μm. Among the studied samples, those meeting the following requirements were selected for SR μCT investigations: i) large dimension and compactness (i.e. material suitable for cylinder extraction); ii) relatively small grain size, ensuring a representative acquisition of the inter- and intra-grain structures in the investigated volume; iii) absence of alteration and/or low-density phases (e.g. amphibole, serpentine); iv) compositional and textural features, unequivocally ascribable to a mantle-derived origin and not to cumulate processes. Among the Antarctica mantle xenoliths, three anhydrous porphyroclastic lherzolites [BR1, BR4 (+BR4B) and BR5] were therefore considered as the most suitable candidates. The grain size variability among the chosen samples and among each of the constituent phases, as well as the absence of amphibole, plagioclase and/or serpentine ensured that representative results were obtained regarding occurrence, volumetric abundance, shape and connectivity of the fluid and melt phases. Sample preparation, tomographic acquisition, 3D image processing and analysis were performed following the method described by Lanzafame et al. (2020). For further technical details, see Supplementary Material files.

3.4. CO_2 measurements in fluid inclusions

The quantification of CO_2 in this suite of samples was performed during the investigation of noble gas (He-Ne-Ar) concentrations in FI (Correale et al., 2019). Based on xenoliths dimensions and the feasibility of hand-picking hundreds of milligrams of crystals, 72 aliquots of pure and unaltered olivine (n. 37), orthopyroxene (n. 21), clinopyroxene (n. 11), and amphibole (n. 3) were separated for measuring the CO_2 amounts in FI. After samples grinding and sieving, crystals without impurities and larger than 0.5 mm were hand-picked following the lab protocol developed at the Istituto Nazionale di Geofisica e Vulcanologia (INGV), Sezione di Palermo, Italy (Rizzo et al., 2018, 2021). In parallel, n. 21 polycrystalline aggregates with diameter between 5 and 10 mm, representative of small portions of the most fine-grained studied samples, were isolated to quantify the bulk CO_2 amount stored as fluid in both inter- and intragranular phases. Mineral aliquots and bulk-rock micro-blocks were then cleaned ultrasonically in 6.5% HNO_3 and in 6.5% HCl, before being rinsed with deionized water and acetone in an ultrasonic bath. Between 0.05 and 1.20 g of sample were loaded into the crusher for analyses. The CO_2 concentration in FI was determined at the Noble gas isotope laboratory of INGV-Palermo in Italy. The selected crystals were loaded into a stainless-steel crusher capable of holding up to six samples simultaneously for noble-gas analysis. FI were released by in-vacuo single-step crushing of minerals at about 200 bars applied by a hydraulic press. The CO_2 estimation was first performed during noble-gas extraction at the time of crushing. This was done by quantifying the total gas pressure ($CO_2 + N_2 + O_2 +$ noble gases) and subtracting the residual pressure of $N_2 + O_2 +$ noble gases after removing CO_2 using a "cold finger" immersed in liquid N_2 at −196 °C. For further details about sample preparation and analytical procedures, see Faccini et al. (2020) and Rizzo et al. (2018, 2021).

4. Petrography, fluid inclusions occurrence and 3D imaging analyses

The studied Greene Point, Baker Rocks and Handler Ridge ultramafic xenoliths (Fig. 1; Table 1) belong to pre-existing collections (see the recent review by Coltorti et al., 2021). Greene Point xenoliths are coarse-grained (grain size 0.2–4.0 mm) protogranular anhydrous harzburgites to lherzolites (Fig. 1). The eleven ultramafic xenoliths selected to represent the variability of the Baker Rocks suite are five anhydrous porphyroclastic lherzolites (grain size 0.5–4.0 mm), two anhydrous porphyroclastic to mosaic equigranular harzburgites (grain size 0.4–3.0 mm), one porphyroclastic olivine-websterite (grain size 0.2–1.5 mm), one porphyroclastic amphibole-bearing lherzolite and two composite samples, made up by porphyroclastic harzburgitic/lherzolitic matrices cut by hornblenditic veins (grain size 0.2–2.5 mm) (Fig. 1). The Handler Ridge samples include three mantle-derived anhydrous lherzolites (grain size 0.2–3.5 mm), as well as one wehrlite (grain size 0.1–3.0 mm) with clear magmatic (cumulitic) origin (Fig. 1) (see Coltorti et al., 2021). Detailed petrographic features are reported in Table 1 and Supplementary Material files.

Table 1
Classification, texture and mineral phase modal abundances in the studied ultramafic xenoliths from northern Victoria Land (Antarctica). For each sample, the main chemical features of the mineral phase constituents are also reported. Lh = lherzolite; Hz = harzburgite; Weh = wehrlite; Ol-Wb = olivine-websterite; Amp-Lh = amphibole-bearing lherzolite; Hb = hornblendite vein; Ol = olivine; Opx = orthopyroxene; Cpx = clinopyroxene; Sp = spinel; Amp = amphibole; * = includes reaction zones, generally composed of secondary phases (cpx, sp., ol) ± glass.

Locality	Sample	Lithotype	Textural type	Modal abundances							Olivine		Orthopyroxene		Clinopyroxene			Spinel		Amphibole	
				Ol	Opx	Cpx	Sp	Amp	Glass/reaction zones*	Tot	*Fo*	NiO (wt %)	Mg#	Al_2O_3	Mg#	Al_2O_3	TiO_2	Mg#	Cr#	Mg#	TiO_2
Greene Point	GP38	Lh	Protogranular	72.7	18.5	8.7	0.1	0.0	traces	100.0	91.7	0.39	92.3	4.0	92.8	5.5	0.3	76.8	42.5	–	–
Greene Point	GP41	Lh	Protogranular	43.7	41.0	11.5	3.8	0.0	traces	100.0	90.5	0.39	91.0	4.1	92.1	4.9	0.1	75.7	22.3	–	–
Greene Point	GP42	Hz	Protogranular	77.9	20.3	1.7	0.1	0.0	traces	100.0	91.8	0.40	92.4	2.5	93.7	3.2	0.1	72.4	47.7	–	–
Greene Point	GP56	Hz	Protogranular	50.0	47.5	1.8	0.7	0.0	traces	100.0	91.7	0.39	92.3	3.9	93.1	5.2	0.2	78.1	28.4	–	–
Baker Rocks	BR1	Lh	Porphyroclastic	62.0	30.0	6.0	2.0	0.0	traces	100.0	89.5	0.42	90.1	3.7	91.8	4.3	0.1	74.4	19.8	–	–
Baker Rocks	BR3	Lh	Porphyroclastic	55.0	24.8	19.0	1.2	0.0	traces	100.0	89.8	0.41	90.3	3.5	91.7	4.4	0.1	75.7	19.1	–	–
Baker Rocks	BR4 (+ BR4B)	Lh	Porphyroclastic	51.0	33.5	10.0	4.7	0.0	0.8	100.0	88.2	0.37	89.5	3.5	90.8	4.3	0.2	68.1	39.9	–	–
Baker Rocks	BR5	Lh	Porphyroclastic	46.5	29.0	20.0	4.5	0.0	0.0	100.0	89.8	0.39	90.3	4.0	91.6	4.8	0.1	76.3	18.5	–	–
Baker Rocks	BR29	Lh	Porphyroclastic	66.2	21.0	9.0	3.8	0.0	traces	100.0	91.1	0.42	91.4	3.4	92.3	4.3	0.1	73.2	32.7	–	–
Baker Rocks	BR38	Hz	Mosaic equigranular	78.5	19.0	1.5	1.0	0.0	traces	100.0	91.7	0.41	92.1	1.2	94.2	1.5	0.0	59.9	59.3	–	–
Baker Rocks	BR42	Hz	Porphyroclastic	64.5	30.0	3.3	2.2	0.0	0.0	100.0	90.6	0.40	91.2	3.4	92.1	4.6	0.3	72.8	30.7	–	–
Baker Rocks	BR47	Ol-Wb	Porphyroclastic	38.3	43.0	16.0	1.7	0.0	1.0	100.0	90.6	0.40	91.0	3.4	92.4	4.1	0.1	74.3	25.4	–	–
Baker Rocks	BR53 Hz	Hz	Porphyroclastic	77.5	18.0	2.3	2.2	0.0	traces	100.0	82.4	0.31	83.9	3.3	86.0	5.3	1.0	57.3	22.2	–	–
Baker Rocks	BR53 Hb	Hb	Ad-cumulitic	0.0	0.0	0.0	0.0	100.0	traces	100.0	–	–	–	–	–	–	–	–	–	80.8	5.2
Baker Rocks	BR55 Lh	Lh	Porphyroclastic	68.0	19.0	11.0	2.0	0.0	traces	100.0	84.4	0.32	85.4	3.7	87.3	5.5	1.0	63.8	20.7	–	–
Baker Rocks	BR55 Hb	Hb	Ad-cumulitic	1.0	0.0	0.0	0.1	98.9	traces	100.0	83.8	0.30	–	–	–	–	–	47.0	46.8	82.6	5.4
Baker Rocks	BR56	Amp-Lh	Porphyroclastic	47.5	18.0	15.0	4.5	15.0	traces	100.0	81.9	0.26	82.7	4.3	84.0	5.4	1.0	49.0	24.4	78.9	4.9
Handler Ridge	HR1	Lh	Protogranular	67.0	21.0	10.0	2.0	0.0	0.0	100.0	89.4	0.39	90.0	4.1	90.1	6.0	0.4	76.3	11.7	–	–
Handler Ridge	HR2	Lh	Protogranular	72.0	17.0	8.0	3.0	0.0	traces	100.0	88.1	0.35	88.8	4.0	88.4	6.1	0.6	70.0	17.9	–	–
Handler Ridge	HR3	Lh	Protogranular	55.0	24.0	17.0	4.0	0.0	0.0	100.0	89.4	0.38	90.0	3.8	91.3	6.0	0.4	77.0	10.1	–	–
Handler Ridge	HR11	Weh	Meso-cumulitic	81.0	0.0	16.0	3.0	0.0	traces	100.0	84.9	0.30	–	–	87.3	4.5	1.2	55.7	29.3	–	–

4.1. FI occurrence and description

Optical microscopy observation on thin sections allowed the determination of the dimension, distribution and typology of FI. In all samples, FI are variably abundant in both olivine and pyroxenes, especially in association with inter-granular reaction zones. Their diameter ranges from a few μm to tens of μm (Fig. 2). Following the classification scheme of Roedder (1984), two main FI genetic types were identified: i) primary, i.e. isolated FI within single grains, and/or FI clusters/trails crossing specific crystals but being unconnected to the neighbouring phases or to the reaction zones (Fig. 2a-h); ii) secondary, i.e. FI aligned within exsolution lamellae in pyroxenes, and/or clusters/trails of FI propagating through neighbouring phases, often accompanied by reaction zones at crystal edges (Fig. 2a-h; see also Faccini et al., 2020; Rizzo et al., 2021).

The Greene Point protogranular lherzolites and harzburgites are generally poor in FI. Trails of secondary FI are the most abundant occurrence: when present, they propagate through orthopyroxene and clinopyroxene (± olivine) (Fig. 2a) and fade into the volumetrically limited reaction zones (see Supplementary Material). Isolated (primary) FI are rare, and usually are smaller than the secondary ones. In the harzburgites, both primary and secondary FI are smaller and less abundant than in the lherzolites.

The Handler Ridge lherzolites are also poor in FI, which are also heterogeneously distributed throughout the samples. Isolated FI occur inside both olivine and orthopyroxene, while FI trails, sometimes cross-cutting each other, are documented especially in olivine and clinopyroxene. No secondary trails propagating through neighbouring phases were identified. An exception is constituted by lherzolite HR2, which is relatively enriched in FI: here, multiple FI trails cross-cut each other and propagate through neighbouring phases, sometimes being associated with melt inclusions (Fig. 2b). The Handler Ridge wehrlite is rich in FI, occurring both isolated and in trails inside single grains of clinopyroxene, and subordinately olivine. In this latter, FI are mostly isolated and concentrated in proximity of the grain edges, often fading into inter-granular areas. Secondary trails propagating through neighbouring olivine are easily visible, while trails propagating between olivine and clinopyroxene are absent.

By contrast, the Baker Rocks xenoliths are very rich in both primary and secondary FI, which occur either isolated within minerals, as trails crossing single grains or concentrated along the grain boundaries, or as trails propagating through neighbouring phases (Fig. 2c-h). In some cases, multiple parallel FI trails within healed cracks or different generations of cross-cutting trails can be observed. Anhydrous porphyroclastic lherzolites are quite rich in FI, present as trails or clusters inside single grains of olivine (Fig. 2c, e) and orthopyroxene or as clusters

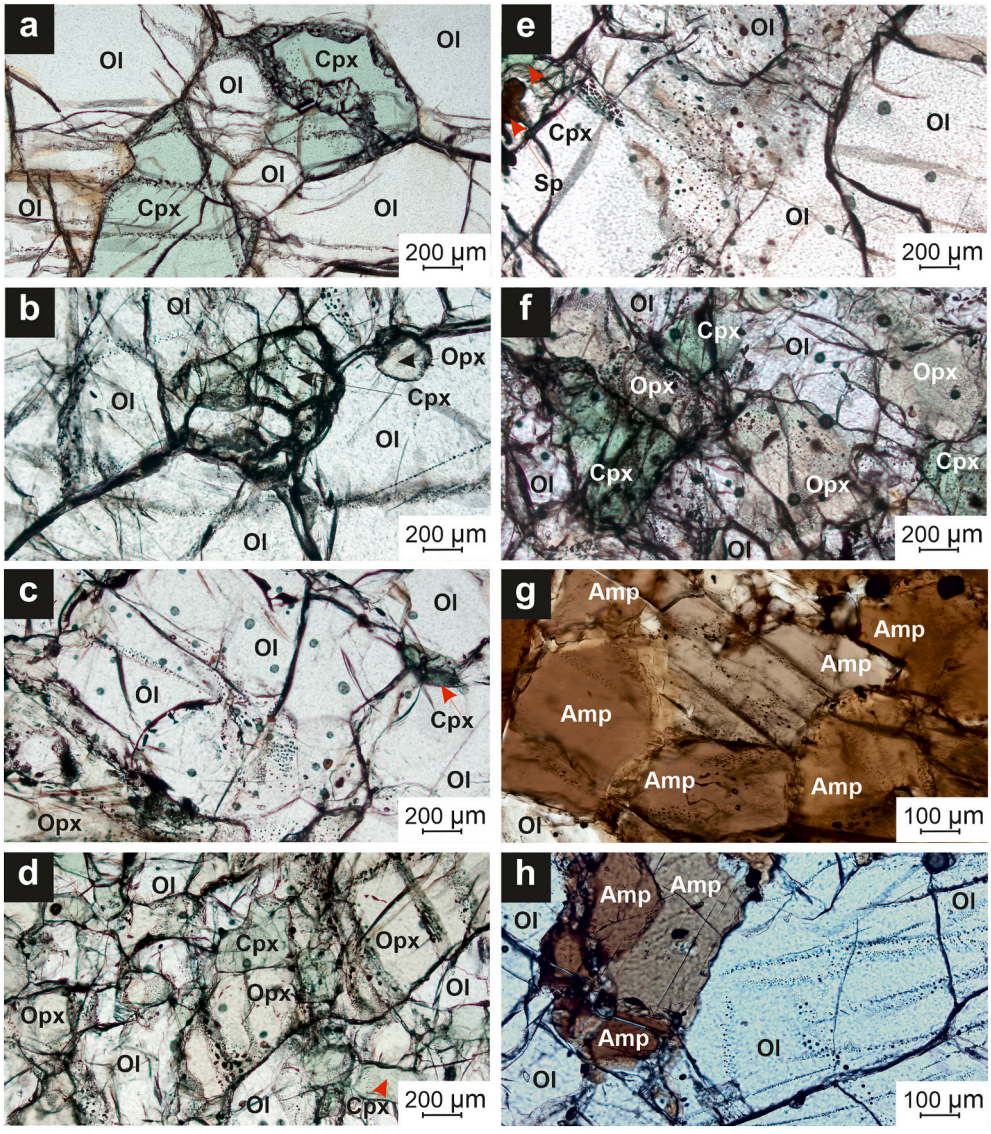

Fig. 2. Photomicrographs in plane-polarized light showing the most representative types and/or associations of fluid inclusions (FI) in the studied northern Victoria Land ultramafic xenoliths. a) Secondary FI trails propagating through olivine and clinopyroxene in Greene Point harzburgite; b) cross-cutting FI trails in olivine and clusters in clinopyroxene in Handler Ridge lherzolite; c) FI clusters and trails in olivine with associated melt inclusions in Baker Rocks anhydrous lherzolite; d) Abundant FI occurring both in trails and clusters in Baker Rocks harzburgite; e) Isolated FI cluster in olivine in Baker Rocks lherzolite; f) Isolated FI clusters in orthopyroxene and clinopyroxene in Baker Rocks harzburgite; g) FI trails propagating through amphibole grains in hornblenditic vein of composite samples from Baker Rocks; h) FI trails cutting olivine in proximity of (but unconnected to) hornblenditic veins in composite samples from Baker Rocks. Ol = olivine; Opx = orthopyroxene; Cpx = clinopyroxene; Amp = amphibole.

inside clinopyroxene. The trails usually fade into intergranular phases or reactions, except some rare cases in which they propagate through neighbouring olivine crystals. In some samples (e.g., BR5 and BR29) the secondary trails are more abundant and often accompanied by the occurrence of μm-sized melt inclusions and/or spinel micro-grains (Fig. 2c). In these cases, multiple generations of FI trails can be identified from their mutual (cross-cutting) relationships. The Baker Rocks porphyroclastic harzburgite is richer in FI than the lherzolites, as is evident from clusters of isolated FI inside pyroxenes, as well as from trails crossing through single grains or the entire paragenesis (Fig. 2d, f). In orthopyroxene, local alignments between FI trails and exsolution lamellae are sometimes visible. Amphibole-bearing xenoliths from the Baker Rocks are equally rich in FI. Amphibole generally hosts numerous FI, both as isolated phases, primary and secondary trails (Fig. 2g). In composite rocks, secondary FI trails propagate through neighbouring amphibole grains in the hornblenditic matrix, and often fade into the glass and/or the contact between the hornblendite veins and the lherzolitic/harzburgitic matrixes. Some secondary FI trails developed through the matrix olivine and orthopyroxene seem to be directly connected to reaction zones between the hornblendite and the lherzolitic/harzburgitic portion (Fig. 2h). No "late-stage" secondary trails propagating through both the matrix and the hornblendite (i.e. post-formation of hornblendite veins) were documented.

4.2. 3D image analyses: glass, voids and connectivity

SR μCT analyses enabled us to identify the mineral phase constituents of lherzolites as well as inter- and intra-granular glasses and voids, confirming the great potential of high-resolution imaging techniques in the characterization of mantle xenoliths (see Créon et al., 2017). As shown in Figs. 3 and S1, glass phases are mostly located at the grain and phase boundaries, where they are organized in veins and/or melt pockets, while fluid phases occur both in intra- and inter-granular (vesicles enclosed by glass) areas. Intra-granular fluid phases are present either as isolated inclusions (Figs. 2, 3, S1) or as inclusion trails (Figs. 2, 3, S1), and are by far easier to isolate than inter-granular fluids, which are often associated with articulated systems of small-scale fractures and cracks (Figs. 3 and S1).

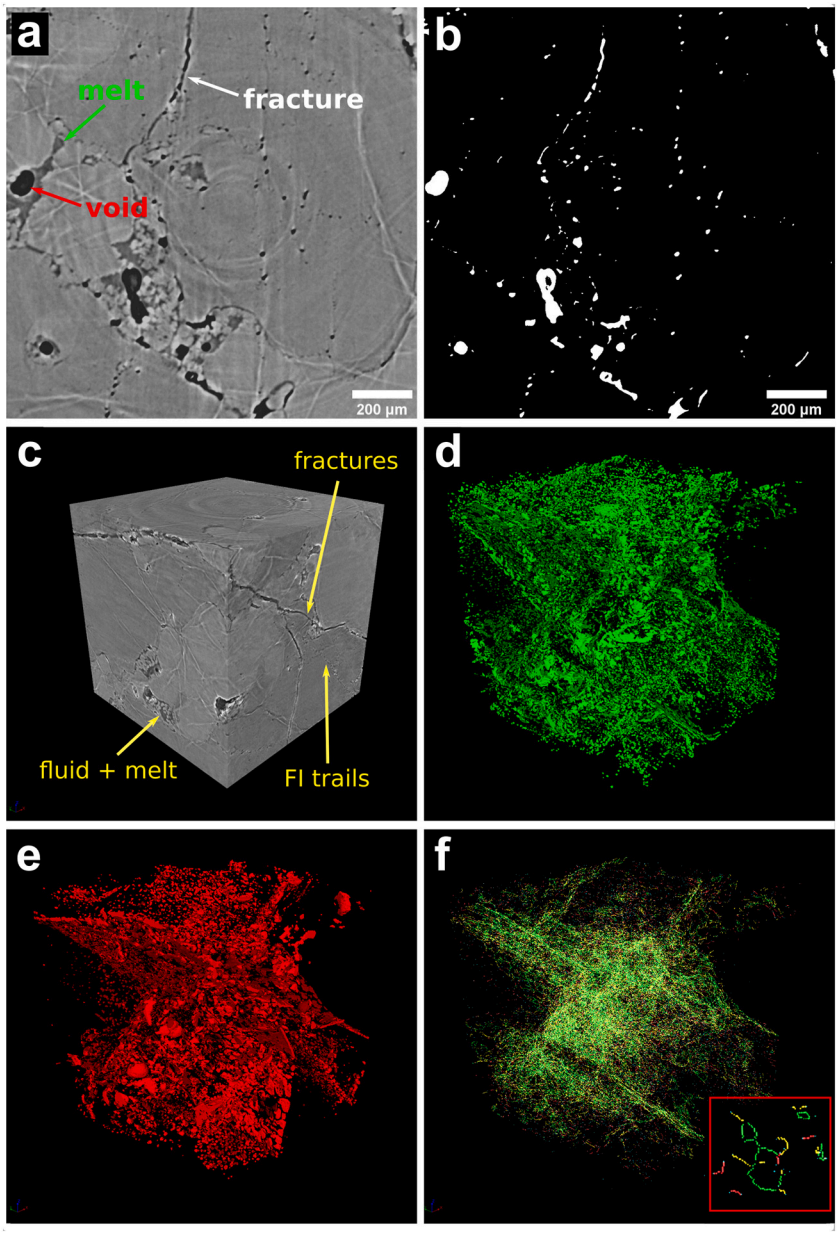

Fig. 3. Results of SR μCT analysis of sample BR4. (a) reconstructed axial slice showing the crystalline phases (light grey, given by pyroxene and olivine), melt (grey) and void (black). Bright lines may be related to small and unresolvable oxides or fractures; (b) binary image showing the segmented void phase (in white); (c) 3D volume renderings of a Volume of Interest (2.57 mm^3) in greyscale; (d) and (e) segmented glass and void phases, respectively; (f) LKC skeleton of the melt phase with the following code colour as shown in the zoomed inset: green = node-to-node, yellow = node-to-end, red = end-to-end. Isotropic voxel size = 1.37 μm. (For interpretation of the references to colour in this figure legend, the reader is referred to the web version of this article.)

Volumetric estimates by image analysis revealed that glass varies between 0.2 and 2.5 vol%, while voids range from 1.1 to 2.3 vol% (Fig. 4a-b; Table 2). Results obtained by skeletonization of segmented sample volumes showed that the volumetric abundance of glass is positively correlated with its connectivity density, which ranges from 323 to 943 mm^{-3}, while voids are less interconnected than glass, as evident from their low connectivity density (4–44 mm^{-3}) (Fig. 4c; Table 2). As expected, the highest number of voids is displayed by lherzolite BR1, where inter-granular fractures are more abundant, while the lowest number of voids characterizes lherzolite BR5. On the other hand, it is interesting to notice how glass and voids are intimately correlated: samples BR1, BR4 and BR4B have the highest glass and voids abundance (2.3–2.5 and 1.3–2.3 vol%, respectively), whereas lherzolite BR5 is typified by extremely low amounts (0.2 vol% glass; 1.1 vol% voids).

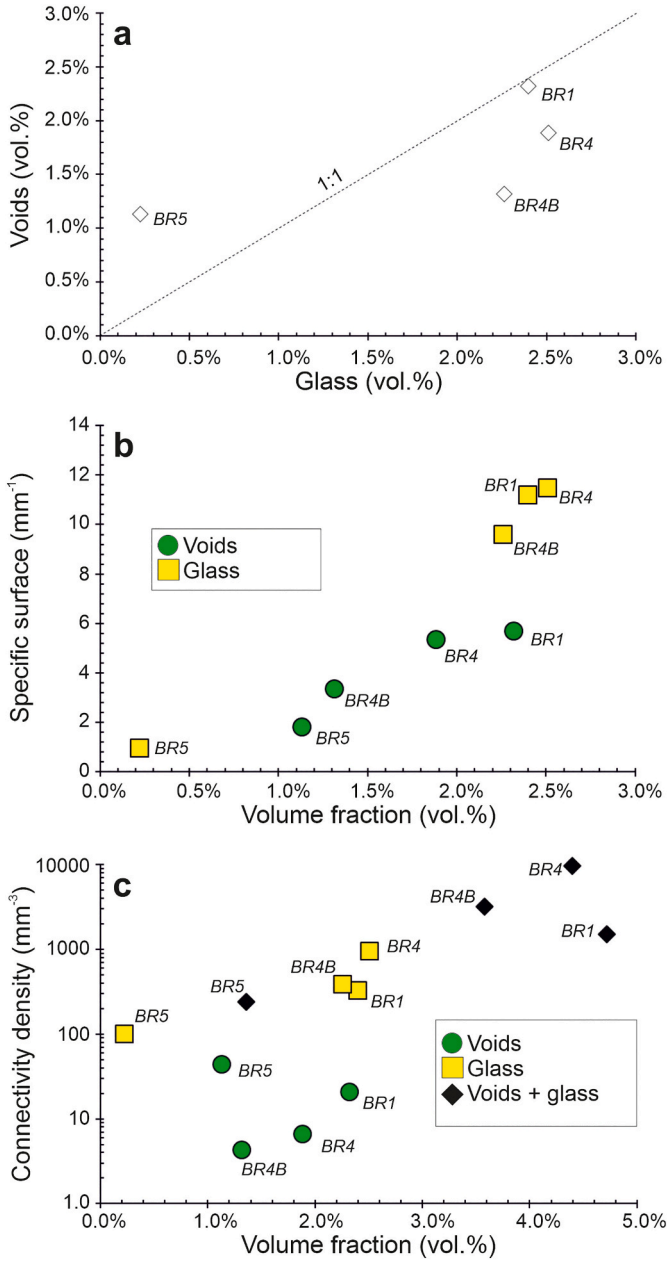

Fig. 4. Volume fraction and 3D parameters (specific surface, connectivity density) of voids and glass phases in northern Victoria Land mantle xenoliths obtained after 3D reconstruction and segmentation of Volume of Interests. (a) volume fraction of voids versus volume fraction of glass; (b) specific surface versus volume fraction of glass and voids phases; (c) connectivity density versus volume fraction of glass, voids and "glass + voids" phases.

5. Mineral and fluid inclusions chemistry

5.1. Mineral chemistry

Although variable between different lithotypes and xenolith suites, the composition of the mineral phase constituents of the studied samples is consistent with those reported from NVL ultramafic xenoliths (Coltorti et al., 2021). For further details, see Supplementary Material files and Supplementary Tables 1–6.

The Greene Point harzburgites and lherzolites are constituted by high forsteritic olivine ($Fo_{90–92}$; NiO = 0.35–0.41 wt%), high-Mg orthopyroxene [Mg# = 91–93, where Mg# = (MgO)/(MgO + FeO) mol%] and high-Mg clinopyroxene (Mg# = 92–94) (Fig. 5a-d). Spinel has Mg# of 72–78 and Cr# [$(Cr_2O_3)/(Cr_2O_3 + Al_2O_3)$ mol%] varying from 22 to 48 (Fig. 5d). The Al_2O_3 content of orthopyroxene and clinopyroxene is 2.5–4.4 and 3.2–5.6 wt%, respectively, while the TiO_2 content of clinopyroxene varies from 0 to 0.3 wt% (Fig. 5a-c). When present, glass ranges from phonolitic to trachytic, and mostly plots in the Na-alkaline field on a CaO + Na_2O vs. TiO_2 + K_2O diagram (Coltorti et al., 2000) (Fig. 5e).

In the Handler Ridge lherzolites, olivine has $Fo_{88–90}$ and NiO contents of 0.33–0.42 wt%, while spinel has Mg# of 70–77 and Cr# of 10–18 (Fig. 5d). The Mg# of orthopyroxene and clinopyroxene is in the range of 88–90 and 87–92, respectively, with corresponding Al_2O_3 contents of 3.2–4.7 wt% and 5.3–7.0 wt% (Fig. 5a-c). In clinopyroxene, the TiO_2 content ranges from 0.2 to 1.1 wt% (Fig. 5b). Glass ranges in composition from trachyandesitic/trachytic to tephriphonolitic/phonolitic, and has a scattered distribution on the CaO + Na_2O vs. TiO_2 + K_2O diagram (Fig. 5e). The wehrlite is composed of Fo_{85} olivine (NiO content down to 0.26 wt%), high-Al spinel (Mg# = 54–58; Cr# = 25–32) and Ti—Cr rich clinopyroxene (Mg# = 86–89; TiO_2 = 1.1–1.3 wt %; Cr_2O_3 = 1.1–1.3 wt%) (Fig. 5a-d).

In the Baker Rocks anhydrous porphyroclastic harzburgite, lherzolites and olivine-websterite, olivine has $Fo_{88–91}$ and NiO content of 0.32–0.54 wt%, while spinel has Mg# of 69–77 and Cr# of 18–40 (Fig. 5d). Orthopyroxene and clinopyroxene have Mg# of 89–92 and 90–93, respectively, for corresponding Al_2O_3 contents of 3.0–4.2 and 3.8–5.0 wt% (Fig. 5a-c). The TiO_2 content of clinopyroxene lies between 0.1 and 0.6 wt% (Fig. 5b). The anhydrous mosaic equigranular harzburgite BR38 has quite different composition, being made of high Fo (92) and NiO (0.37–0.43 wt%) olivine coexisting with high-Cr# (59–60) spinel. Orthopyroxene and clinopyroxene have high-Mg# (~92 and 93–95, respectively) and low-Al_2O_3 (0.8–1.3 and 1.4–1.6 wt%) (Fig. 5a-c). The amphibole-bearing lherzolite and the composite samples (harzburgite-lherzolite + hornblendite veins) are made of low Fo (81–85) and NiO (0.25–0.36 wt%) olivine; spinel has Cr# of 20–25 and Mg# of 47–65 (Fig. 5d). The Mg# of orthopyroxene and clinopyroxene are 82–86 and 82–88, respectively, with corresponding Al_2O_3 contents of 2.5–5.6 and 4.7–6.2 wt% (Fig. 5a-c). Amphibole in the hornblenditic veins of the composite samples has Mg# of 80–83, TiO_2 = 5.0–5.4 wt%, Na_2O = 2.7–3.1 wt%, K_2O = 0.9–1.0 wt%, and Cr_2O_3 = 0.1–0.7 wt%, while in the amphibole-bearing peridotites, a less magnesian (Mg# = 79) and more chromiferous (Cr_2O_3 = 1.0 wt%) amphibole occurs, mostly associated with reaction zones. When present, glass is basaltic to trachybasaltic (Fig. 5e).

5.2. Chemistry of FI

Hereafter, the CO_2 distribution in FI in mineral phases and/or bulk rocks from NVL ultramafic xenoliths is quantified as μg/g, that is the abbreviation for $\mu g_{(CO2)}/g_{(sample)}$. Such expression, derived from the conversion of the original moles of CO_2 measured per gram of sample (mol/g, Table 3; Supplementary Tables 7–8), was adopted to compare

Table 2
Results of 3D analyses of mantle xenoliths from northern Victoria Land performed on Volumes of Interest (VOI) after scan acquisition via Synchrotron radiation computed microtomography (SR μCT) measurements. Segmentation for basic analysis on the voids and glass phases (retrievement of volume fractions) was performed on VOI of 1000 × 1000 × 1000 voxels, while skeletonization for the investigation of connectivity density was performed on VOI of 500 × 500 × 500 voxels.

Sample	Volume (Voxels)	Volume (mm^3)	Phase	Euler number (mm^{-3})	Connectivity density	Integral of mean curvature (mm^{-2})	Specific Surface (mm^{-1})	Volume fraction (vol%)
BR1	1000 × 1000 × 1000	2.571	Glass	10,804.532	323.560	1433.153	11.189	2.40
			Voids	2978.570	20.610	475.501	5.669	2.32
			Glass + Voids		1522.150			4.72
			Spinel	1236.130		115.072	0.817	0.23
BR4	1000 × 1000 × 1000	2.571	Glass	12,401.086	943.470	1497.897	11.479	2.51
			Voids	4141.757	6.610	511.276	5.352	1.88
			Glass + Voids		9588.720			4.39
			Spinel	1539.604		175.106	1.308	0.29
BR4B	1000 × 1000 × 1000	2.571	Glass	9931.947	383.840	1166.364	9.583	2.26
			Voids	2152.403	4.270	270.955	3.339	1.32
			Glass + Voids		3221.260			3.58
			Spinel	890.919		89.159	0.616	0.14
BR5	1000 × 1000 × 1000	2.571	Glass	752.054	99.870	107.300	0.940	0.22
			Voids	204.786	44.000	68.285	1.796	1.13
			Glass + Voids		241.000			1.36
			Spinel	137.304		16.179	0.272	0.29

our results to measurements of volatiles in minerals (hydrous phases or NAMs) and/or glass/fluid phases, usually expressed as wt% or ppm. Although apparently implicit, readers are advised that the conversion of μg/g unit into ppm is not legitimate, as the adopted μg/g represents the ratio of a gaseous (grams of CO_2) over a solid phase (grams of mineral or rock), being not directly comparable with ppm fractions by weight or by volume. The reported data, therefore, represent the averaged amount of CO_2 that is stored as fluid in FI hosted in olivine, pyroxenes and amphibole, or, alternatively, as FI + inter-granular fluids in bulk rocks (see Table 3).

Olivine is the phase with the lowest CO_2 contents, being capable of storing between 0.1 and 39 μg/g CO_2, in accordance with the optical observations of FI (Section 4.1). Among the different xenolith suites, the Greene Point lherzolites and harzburgites contain the most CO_2-depleted olivine (0.1–0.5 μg/g). In the Handler Ridge lherzolites, olivine has slightly higher CO_2 concentrations (0.1–1.3 μg/g), while in the wehrlite it can store between 0.1 and 0.2 μg/g of CO_2. The Baker Rocks samples are quite heterogeneous, as the CO_2 contents in olivine in anhydrous porphyroclastic lherzolites and harzburgite span from 0.7 to 19.7 μg/g. Olivine in the Baker Rocks olivine-websterite (0.1–1.4 μg/g) and anhydrous mosaic-textured harzburgite (0.1–0.3 μg/g) is exceptionally CO_2-poor. Amphibole-bearing samples have the most gas-enriched olivine, with CO_2 contents between 7.1 and 38.9 μg/g (Fig. 6a-b; Table 3). The behaviour of olivine among the various populations is mirrored by pyroxenes, although the latter have higher contents of CO_2 stored in their FI. Orthopyroxene and clinopyroxene from the Greene Point lherzolites/harzburgites have CO_2 contents ranging from 0.3 to 2.6 μg/g and from 0.8 to 7.5 μg/g, respectively. Pyroxenes from the Handler Ridge lherzolites are relatively gas-enriched, having CO_2 contents between 0.5 and 11.8 μg/g (orthopyroxene) and between 2.2 and 35.7 μg/g (clinopyroxene). The Baker Rocks samples are typified by the highest amounts of CO_2 in FI. Orthopyroxene and clinopyroxene in anhydrous porphyroclastic lherzolites and harzburgites can store 8.1 to 114.6 and 7.9 to 73.1 μg CO_2 per gram of sample, respectively. The low concentration of CO_2 stored in orthopyroxene FI (18.4 μg/g) from the olivine-websterite further testifies that it is relatively gas-depleted. Orthopyroxene in amphibole-bearing samples (BR53, BR55, BR56) is extremely rich in CO_2 containing from 41.6 up to 187.3 μg/g (Fig. 6a-c; Table 3). The high abundance of amphibole in samples BR53 and BR56 enabled the measurement of the concentration of CO_2 stored in its FI, which spans from 14.2 to 42.8 μg/g (Table 3). The amounts of CO_2 measured after crushing of the bulk xenoliths is in line with the concentrations released from the single phases: the Greene Point bulk lherzolites and harzburgites contain from 0.3 to 11.2 μg/g CO_2 in FI and inter-granular fluids, while the Handler Ridge lherzolites have CO_2 contents up to 2.4 μg/g. The Baker Rocks anhydrous porphyroclastic lherzolites have CO_2 contents between 2.1 and 57.2 μg/g, while amphibole-bearing rocks contain from 30.9 to 42.0 μg/g CO_2 (Table 3).

6. Thermal and redox state of the Antarctica SCLM

Equilibration T and fO_2 conditions recorded by the studied ultramafic xenoliths were calculated by using the two-pyroxene thermometer of Brey and Kohler (1990) ($T_{[BKN90]}$) and the olivine-spinel-orthopyroxene oxygen barometer of Miller et al. (2016). For sample HR11 (orthopyroxene-free wehrlite), the Ballhaus et al. (1991) olivine-spinel thermometer and olivine-spinel oxy-barometer were used. Input pressures were set at 1.1, 0.8 and 0.9 GPa for Greene Point, Baker Rocks and Handler Ridge xenoliths respectively, following Coltorti et al. (2021) (see Supplementary Material files for further details).

All the obtained T-fO_2 results (Fig. 7; Table 4) are fairly consistent with the systematics reported by previous studies on the same xenolith suites (see Coltorti et al., 2021). The Greene Point lherzolites and harzburgites record the highest T (1010–1070 °C) and the lowest fO_2 values (from −1.4 to −3.1 $\Delta \log fO_2$ [FMQ], with FMQ = Fayalite-Magnetite-Quartz) (Fig. 7; Table 4). As this xenoliths population also records the highest P (0.8–1.6 GPa), it can be inferred that quite reduced conditions prevailed in the deepest portion of the SCLM beneath NVL. The Baker Rocks anhydrous porphyroclastic harzburgites, lherzolites and olivine-websterite record T between 861 and 990 °C, at relatively low oxygen fugacity values (from −0.7 to −2.1 $\Delta \log fO_2$ [FMQ]). The mosaic equigranular harzburgite (BR38) record significantly lower T (~800 °C) and higher fO_2 (+0.3 $\Delta \log fO_2$ [FMQ]) with respect to the porphyroclastic rocks. The amphibole-bearing samples yield variable T (905–990 °C) but, at the same time, more oxidized fO_2 values (from

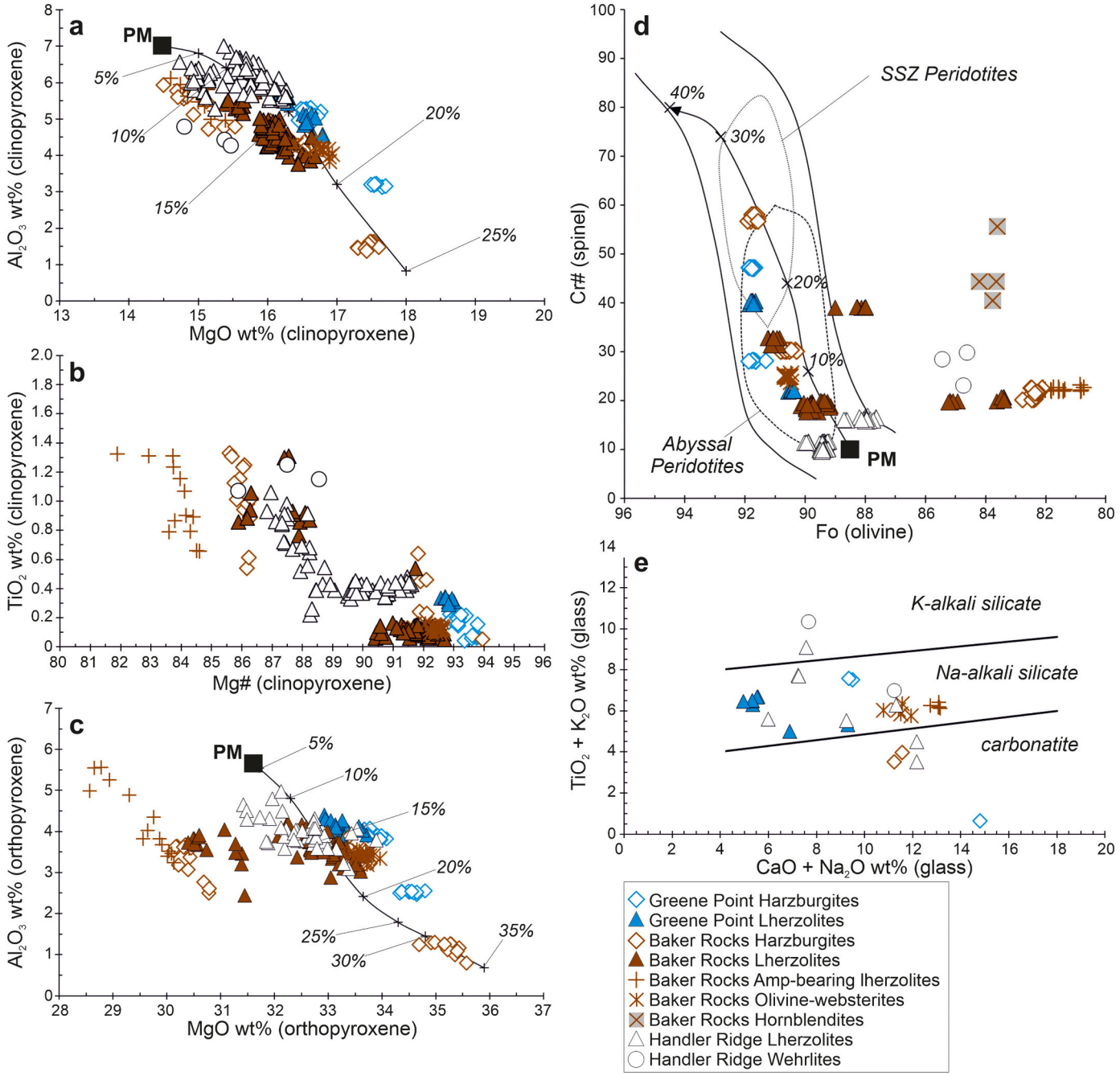

Fig. 5. Major element composition of the main phase constituent of northern Victoria Land ultramafic xenoliths: (a) Al_2O_3 (wt%) versus MgO (wt%) in clinopyroxene; (b) TiO_2 (wt%) versus Mg# in clinopyroxene; (c) Al_2O_3 (wt%) versus MgO (wt%) in orthopyroxene; (d) Olivine-spinel mantle array (OSMA) diagram (Arai, 1994); (e) $TiO_2 + K_2O$ (wt%) vs. $CaO + Na_2O$ (wt%) in glasses (Coltorti et al., 2000). The melting curves in (a) and (c) are developed as in Melchiorre et al. (2020); (see references therein). Numbers and thick marks correspond to melt extracted percentages. In (d), Primitive Mantle (PM) composition of olivine and spinel was calculated as in Rizzo et al. (2021; see references therein). The black arrow refers to the melting model of Arai (1994); numbers and thick marks correspond to melt extracted percentages. Compositional fields of Supra-Subduction Zone (SSZ; Pearce et al., 2000) and Abyssal Peridotites (Dick and Bullen, 1984) are also shown for comparison.

−0.7 to +0.3 $\Delta\log fO_2$ [FMQ]) (Fig. 7; Table 4). The Handler Ridge rocks yield the highest fO_2 values (from +0.4 to +0.6 $\Delta\log fO_2$ [FMQ]), at comparable T (830–1040 °C), confirming that this portion of the SCLM is the most oxidized.

7. Discussion

7.1. Relationships between voids and glasses in ultramafic xenoliths

Intra- and inter-granular voids and glasses in mantle xenoliths are the best candidates for tracing the circulation of fluids and melts within the lithospheric mantle, as they play an important role in storing volatiles. The fluid phases are the main host for CO_2 in spinel peridotites ($P < 1.7$ GPa), while at greater depth in the lithosphere and in the asthenosphere,

Table 3
Concentration of CO_2 (μg/g) in bulk samples, as well as in olivine-, orthopyroxene-, clinopyroxene- and amphibole-hosted fluid inclusions in ultramafic xenoliths from northern Victoria Land (Antarctica). For each sample, the bulk CO_2 concentration calculated by weighting the CO_2 content of single phases for their modal abundances is also reported, together with the difference between measured and calculated bulk CO_2 (see text for further explanation). Lh = lherzolite; Hz = harzburgite; Weh = wehrlite; Ol-Wb = olivine-websterite; Amp-Lh = amphibole-bearing lherzolite; Hb = hornblendite vein; Ol = olivine; Opx = orthopyroxene; Cpx = clinopyroxene; Amp = amphibole.

Locality	Sample	Lithotype	CO_2 concentration (μg/g)						
			Ol	Opx	Cpx	Amp	Bulk rock measured	Bulk rock weighted	Bulk measured - weighted (absolute)
Greene Point	GP38	Lh	0.1	0.4	0.8	–	0.4	0.3	0.2
Greene Point	GP41	Lh	0.5	2.3	7.5	–	11.2	2.0	9.1
Greene Point	GP42	Hz	0.1	0.4	–	–	0.3	0.2	0.2
Greene Point	GP56	Hz	0.4	2.6	5.9	–	–	–	–
Baker Rocks	BR1	Lh	15.9	58.5	73.1	–	21.1	31.8	−10.6
Baker Rocks	BR3	Lh	3.5	16.6	11.1	–	–	–	–
Baker Rocks	BR4	Lh	9.6	24.4	20.1	–	39.4	15.1	24.3
Baker Rocks	BR4B	Lh	9.6	24.4	20.1	–	16.8	15.1	1.7
Baker Rocks	BR5	Lh	3.1	28.5	7.9	–	6.7	9.7	−3.0
Baker Rocks	BR29	Lh	1.0	8.1	9.4	–	–	–	–
Baker Rocks	BR38	Hz	0.1	–	–	–	–	–	–
Baker Rocks	BR42	Hz	19.7	114.6	–	–	–	–	–
Baker Rocks	BR47	Ol-Wb	0.8	18.4	7.8	–	–	–	–
Baker Rocks	BR53 Hz	Hz	17.5	41.6	–	–	30.9	21.1	9.8
Baker Rocks	BR53 Hb	Hb	–	–	–	22.0	–	–	–
Baker Rocks	BR55 Lh	Lh	7.1	42.0	–	–	–	–	–
Baker Rocks	BR55 Hb	Hb	–	–	–	–	–	–	–
Baker Rocks	BR56	Amp-Lh	38.9	162.3	–	42.8	42.0	54.1	−12.2
Handler Ridge	HR1	Lh	0.7	9.5	2.2	–	0.6	2.7	−2.1
Handler Ridge	HR2	Lh	0.4	11.8	35.7	–	2.4	5.1	−2.7
Handler Ridge	HR3	Lh	0.1	0.5	2.5	–	0.0	0.6	−0.6
Handler Ridge	HR11	Weh	0.2	–	–	–	–	–	–

CO_2 migrates more easily as a dissolved component of carbonated melts (see Frezzotti and Touret, 2014; Olafsson and Eggler, 1983). The bulk CO_2 content measured in NVL xenoliths varies from 0 to 11 μg/g in the Handler Ridge and Greene Point and up to 2–57 μg/g in the Baker Rocks (Table 3). Similar orders of magnitude are obtained by weighting the amount of CO_2 released from mineral-hosted FI balanced with the modal abundances of mineral phases inside the selected xenoliths (Handler Ridge and Greene Point 0–5 μg/g CO_2; Baker Rocks 10–54 μg/g CO_2) (Table 3). In 50% of the cases (all Greene Point and 50% of Baker Rocks xenoliths), the difference between the CO_2 amount released from the bulk xenoliths and that calculated from the amounts measured in the single mineral phases is positive, while in the remnant peridotites (all Handler Ridge and 50% of Baker Rocks ones) it is negative (Table 3). These results are good proxies for determining the mutual role played by inter- and intra-granular structures for storing CO_2: the positive balance in the Greene Point rocks would indicate that CO_2 was efficiently stored in intergranular fluids, while the negative values obtained for the Handler Ridge xenoliths are consistent with a storage occurring mostly in mineral-hosted FI. In the Baker Rocks samples, it is likely that the storage of CO_2 was heterogeneously distributed between inter- and intra-granular structures.

According to SR μCT results, the mantle xenoliths contain between 1.1 and 2.3 vol% of voids, and 0.2–2.5 vol% of glass (Fig. 4). To quantify the distribution of inter- vs. intra-granular fluids, as well as to understand if void and glass identified by SR μCT can be representative of fluids and melts originally preserved in the SCLM, the effects of secondary processes, such as late mechanical disaggregation after xenoliths entrainment into the host basalt, must be addressed. Indeed, the presence of CO_2-rich fluids exsolved from a melt phase (either generated from hydrous phases breakdown or from infiltration of metasomatic agents), or even unrelated to melts, combined with the anisotropic elastic properties of the mineral constituents, can cause a inhomogeneous internal stress state in mantle xenoliths, and thus induce mechanical failure by the opening of micro-cracks at $P < 200$ MPa, if decompression is faster than the minerals' viscous relaxation rates (Brett et al., 2015; Klügel, 1998).

In the NVL xenoliths, the occasional presence of healed cracks filled by FI trails suggests that fluid infiltration was accompanied by microfracturing (Brett et al., 2015), although the high interconnectivity between voids and glasses indicates that most of the measured voids represent fluid phases rather than secondary cracks. This is confirmed by the positive correlation between the volumetric abundance of the "voids + glass system" and its connectivity density (Fig. 4c), that likely indicates that voids are mostly filled by fluids exsolved from a melt phase. Further confirmations are given by the increase in absolute connectivity density from the single phases (max. ~1000 mm^{-3} glass; max. ~50 mm^{-3} voids) to the "voids + glass system" (up to ~10,000 mm^{-3}), as well as by the positive correlation between the voids volume and the average CO_2 contents in the bulk xenoliths for which SR μCT data are available, which ranges from 7 to 39 μg/g on average (Fig. 8). As is evident from Fig. 8a, the average CO_2 concentration in bulk xenoliths is negatively correlated with the connectivity density of the voids phase, which decreases from 44 to 7 mm^{-3}. An opposite trend characterizes the glass phase, and most importantly by the voids + glass system, which in these samples show a strong positive correlation with CO_2, increasing from 241 up to 9589 mm^{-3} (Fig. 8a). From these results, some speculations about the likely role played by decompression-induced cracking in NVL mantle xenoliths can be made. In fact, the sample having the highest bulk CO_2 content (BR4, max. 57 μg/g; average 39 μg/g CO_2), the highest volume of glass (up to 2.5 vol%) and voids (up to 2.4 vol%), is typified by a poorly connected void phase, but at the same time by an extremely well connected "voids + glass" system (Figs. 4 and 8a-b). Such organization may be achieved when multiple isolated voids filled with CO_2 were immersed in a common, efficiently connected melt, from which the fluid phase likely exsolved once mantle xenoliths decompressed to relatively low P (<200 MPa). On the other hand, the sample having the lowest bulk CO_2 amount (BR5, 7 μg/g CO_2), and the lowest glass (0.2 vol%) and voids (1.1 vol%) fractions is also characterized by a moderately connected voids phase and by the lowest connectivity density of the "voids + glass" system (Figs. 4 and 8a-b). These features can indicate that the CO_2 storage occurred in a melt-poor system, and that the fluid phase was organized to moderately coalescent, as can happen in FI trails inside mineral phases. The negative balance between the CO_2 concentration released from the bulk xenoliths and that calculated from

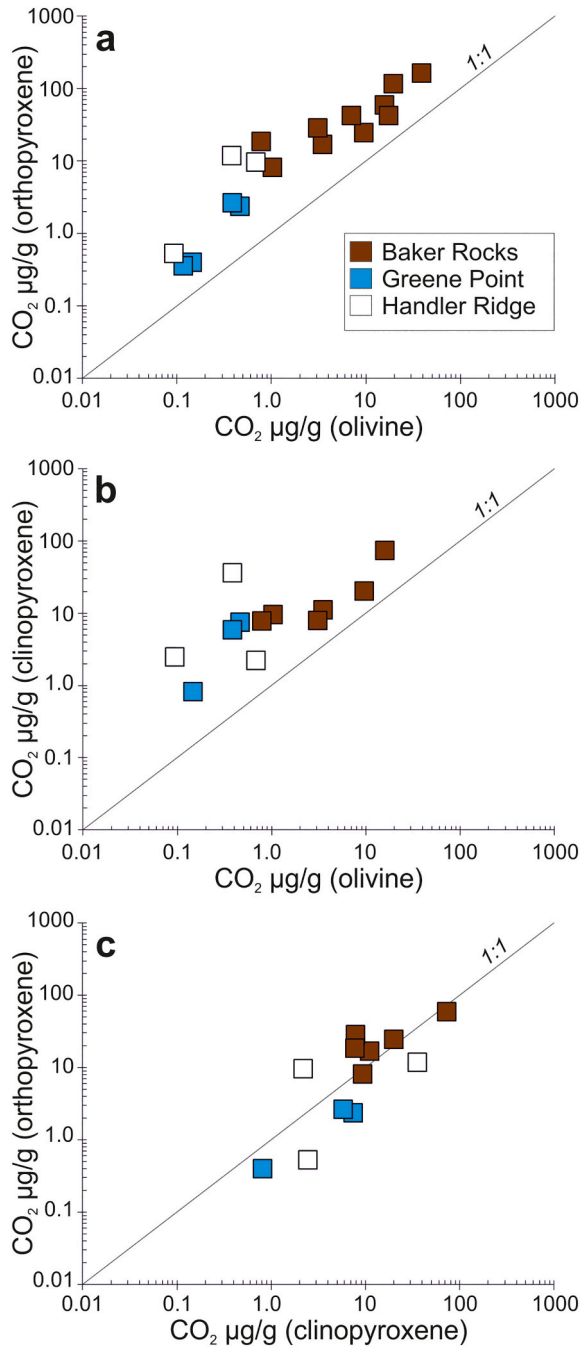

Fig. 6. Absolute concentration (µg/g) and partitioning of CO_2 between olivine and pyroxenes in northern Victoria Land mantle xenoliths. (a) orthopyroxene- and olivine-, (b) clinopyroxene- and olivine-, and (c) orthopyroxene- and clinopyroxene-hosted fluid inclusions. In each panel, the line representing the 1:1 partitioning ratio is reported for comparison.

the amounts measured in the single mineral phases confirms the subordinate role played by inter-granular structures in storing CO_2 in this sample. In any case, among the samples investigated by SR µCT, lherzolite BR5 could be considered as the best approximation of the conditions of storage of fluids and melts in the SCLM prior to xenoliths entrainment by the host basalt.

The good correlation between the CO_2 released from the studied xenoliths and the connectivity of the glass and/or voids phases is in partial contrast with what was found by Créon et al. (2017) for mantle xenoliths from the Pannonian Basin. These authors suggested that the glass (+vesicle) network pervading the samples were connected to the exterior, inducing the loss of volatiles during exposure of the rocks to surface conditions. Although we cannot exclude a priori that some external portions of the xenoliths studied in our work could have been exposed to the surface, the systematic relationships between voids, glasses and the corresponding connectivity (Fig. 4) make us confident that the obtained results mirror a sequence of processes that took place before/during xenoliths entrainment by the host basalt. A similar model was proposed for Gobernador Gregores (Patagonia) mantle xenoliths by Scambelluri et al. (2009), who hypothesized that the FI were entrapped into minerals in strict association with the progressive degassing of alkali basalts during ascent, or, alternatively, by melting of peridotite-forming hydrous phases during xenoliths decompression and concomitant CO_2-fluxing. As already modelled by Coltorti et al. (2004) and Perinelli et al. (1998), glasses in the studied NVL represent a melt phase that infiltrated the xenoliths shortly before their entrainment by the host basalt, generated as product of the reaction induced by the infiltration of alkaline metasomatic agents into the local SCLM.

7.2. *Storage of CO_2 in the Antarctica SCLM*

7.2.1. *The impact of depletion and enrichment processes on the CO_2 distribution in the SCLM*

The concentration of volatiles trapped in FI is strongly dependant on the density of FI within each crystal and the entrapment *P* (Frezzotti et al., 2002), therefore a careful evaluation of the CO_2 distribution within the studied samples must be made in order to filter the results for eventual dependencies on depth and/or degassing processes. Recent studies, comparing the composition of the FI to those of the host minerals in various mantle xenolith suites, highlighted that some CO_2/noble gases ratios (i.e. $^4He/CO_2$ and $^4He/^{40}Ar^*$) may vary with the melting degree and/or metasomatism/refertilization, irrespective of the depth of provenance of the xenoliths (Faccini et al., 2020; Rizzo et al., 2018, 2021).

In the case of NVL xenoliths, when the CO_2/noble gases ratios in FI is plotted versus the Mg# of the host minerals (Fig. 9a-f), samples can be grouped into: i) an end-member with high Mg# (90–93), low $^4He/CO_2$ and low $^4He/^{40}Ar^*$ ratios mainly composed of Greene Point orthopyroxene and clinopyroxene in mantle xenoliths; ii) a vertical trend, constituted by the majority of the mantle-derived samples and typified by increases in $^4He/CO_2$ and $^4He/^{40}Ar^*$ at almost constant Mg#; and iii) a cluster made by cumulitic samples (Mg# <88), with gas systematics typical of mantle production ratios and magmatic values (Fig. 9e-f). Similar indications arise from the comparison between the absolute concentration of CO_2 in FI and the Mg# of the host minerals from each xenolith suite, as shown by the four discrete groups: i) a Mg-rich (Mg# >90), CO_2-poor (<1.5 µg/g) end-member, mostly represented by olivine in Greene Point and some Baker Rocks anhydrous mantle xenoliths; ii) a cluster with lower Mg# (85–89) but comparable CO_2 (0–1.3 µg/g) contents, composed of olivine in cumulates and some mantle rocks from the Handler Ridge; iii) a group with Mg# of 88–93 and CO_2 from 0.32 up to 115 µg/g, that is constituted of most of the olivine in the Baker Rocks and by orthopyroxene/clinopyroxene from all mantle xenolith suites; iv) a group with low Mg# (79–85) but high CO_2 (7–187 µg/g), comprising olivine, orthopyroxene and amphibole belonging to the amphibole-bearing Baker Rocks samples (Fig. 9a). By plotting CO_2 in FI against the TiO_2 and Al_2O_3 (wt%) content of pyroxenes, samples from the different xenolith suites lie on two discrete trends: one composed of the Greene Point and Handler Ridge samples, whose TiO_2 and Al_2O_3 contents are positively correlated with CO_2; another defined by pyroxenes from the Baker Rocks xenoliths, whose CO_2 variations are accompanied by TiO_2 enrichment, at almost constant Al_2O_3 contents (Fig. 9b-c). The $^4He/CO_2$ and $^4He/^{40}Ar^*$ distributions clearly indicate a mantle origin of the gases in the Handler Ridge and Greene Point FI, while the distribution of olivine and most of the pyroxenes in the Baker Rocks samples is within the mantle production ranges but typical of magmatic values ($^4He/^{40}Ar^* > 1$; $^4He/CO_2 > 1.4 \times 10^{-5}$; Fig. 9e-f). Such differences in the

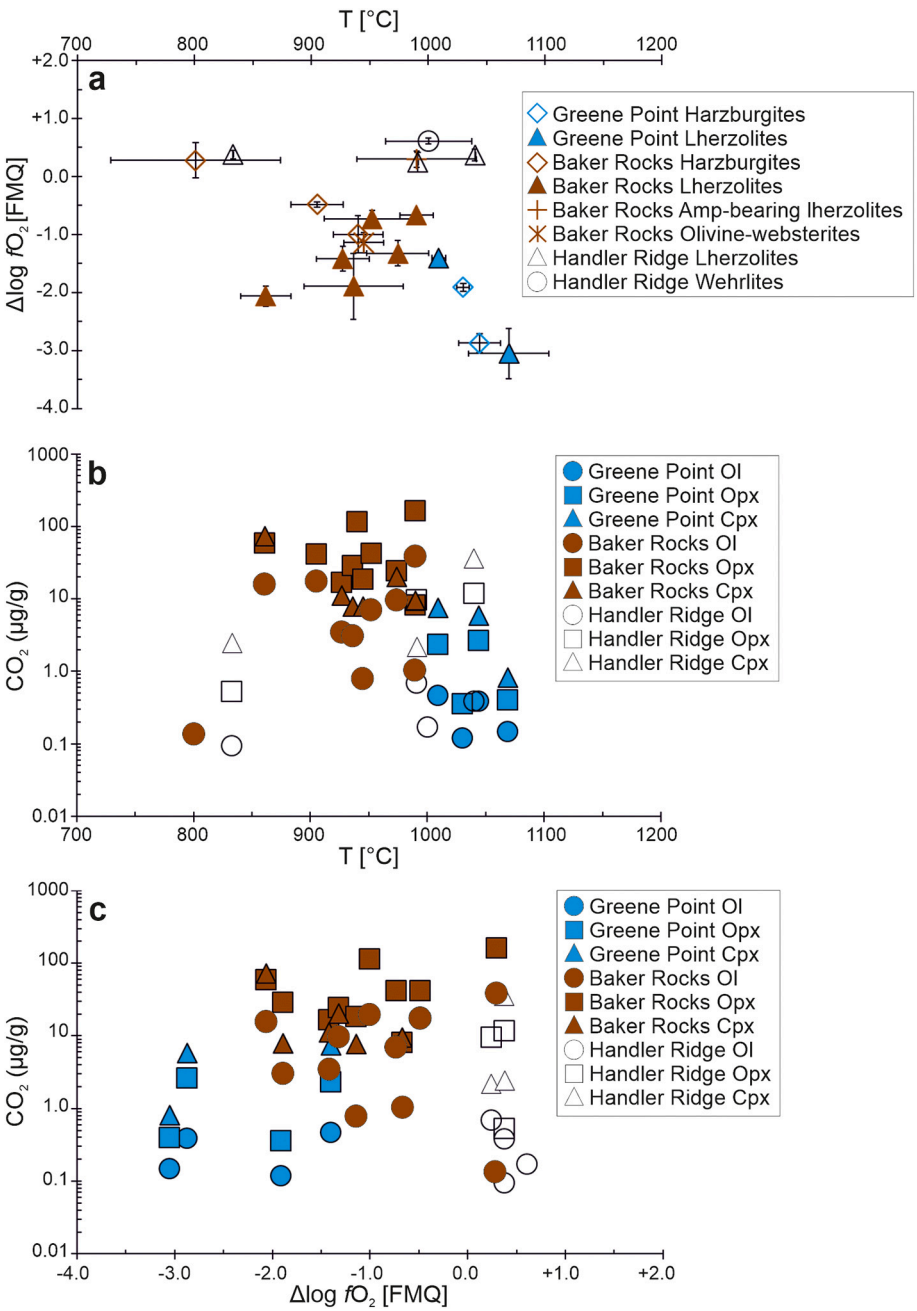

Fig. 7. (a) Temperature (T; °C) versus oxygen fugacity ($\Delta\log fO_2$ [FMQ]) diagram showing the equilibrium conditions recorded by northern Victoria Land ultramafic xenoliths. For each sample, average values ± standard deviations on results obtained from multiple mineral pairs are reported. (b) Temperature (T; °C) versus CO_2 concentration (μg/g) in mineral-hosted fluid inclusions. (c) Oxygen fugacity ($\Delta\log fO_2$ [FMQ]) versus CO_2 concentration (μg/g) in mineral-hosted fluid inclusions. See text for details about calculations of T-fO_2 parameters.

FI ratios could be explained by the differential depths at which the FI entrapment took place, i.e. assuming that the FI in the Baker Rocks samples were trapped from melts degassing at shallower depths than those circulating at Handler Ridge and Greene Point. This is due to the solubility differences between ^{4}He, CO_2 and ^{40}Ar* (He>CO_2> > Ar) in silicate melts, that lead to increasing ^{4}He/CO_2 and ^{4}He/^{40}Ar* values during melts degassing and depressurization (e.g., Boudoire et al., 2018 and references therein). However, this does not seem to be the case for the Antarctica samples, as the highest concentration of CO_2 in the Baker Rocks samples correspond to the shallowest depths of provenance of these xenoliths (0.7–1.1 GPa; Coltorti et al., 2021). In fact, the CO_2 vs. T-P distribution rules out any eventual dependency of the CO_2 measured in the FI on their entrapment depth: if this were the case, an opposite behaviour would be expected, with the deeper Greene Point mantle being richer in CO_2 than the shallower domains. On the other hand, the existence of different clusters and/or trends based on the relationships between CO_2 contents and mineral chemistry (Fig. 9a-c) seems to indicate that the CO_2 stored in the FI is strictly related to the composition of the host minerals (i.e. fertile vs. depleted), and thus to the nature of the metasomatic agent/s that infiltrated the SCLM, rather than to a simple "layering" of the lithospheric mantle and/or to the degree of degassing due to depressurization.

Similar evidence arises from the relationships between the T-fO_2 conditions of last equilibrium recorded by the xenoliths and the CO_2 content of the FI (Fig. 7b-c). In fact, CO_2 is negatively correlated with the equilibrium T-P and positively correlated with fO_2, moving from the most gas-depleted, high-T-P and low-fO_2 Greene Point rocks (1010–1070 °C; 0.8–1.6 GPa; −1.4 to −3.1 $\Delta\log fO_2$ [FMQ]) to the "cooler", shallower and more oxidized samples from the Baker Rocks (860–990 °C; 0.7–1.1 GPa; −0.5 to −2.1 $\Delta\log fO_2$ [FMQ]) (Fig. 7b-c) (see also Coltorti et al., 2021). Exceptions are constituted by one lherzolite from Handler Ridge, as well as by the mosaic equigranular harzburgite

Table 4
Thermobarometric and oxybarometric conditions of last equilibrium recorded by the studied ultramafic xenoliths from northern Victoria Land. Equilibrium *T* (°C) were calculated by means of Brey and Kohler (1990) two pyroxene thermometer (BKN90); olivine-spinel equilibrium *T* (°C) were also obtained with Ballhaus et al. (1991) thermomether (B91). Oxygen fugacity (fO_2, reported as $\Delta\log fO_2$ [FMQ]) was calculated using Miller et al. (2016) oxybarometer; Ballhaus et al. (1991) oxybarometer was used for HR11 xenolith (orthopyroxene-free paragenesis). Input *P* for thermometry and oxybarometry are from Coltorti et al. (2021) as averages for each xenolith population. For each sample, average value and standard deviation (*St.* Dev.) of the results are reported. Hz = harzburgite; Lh = lherzolite; Weh = wehrlite; Ol-Wb = olivine websterite; Amp-Lh = amphibole-bearing lherzolite; Opx = orthopyroxene: Cpx = clinopyroxene; Ol = olivine; Sp = spinel.

Locality	Sample	Lithotype	*T* (Opx-Cpx; °C)		*T* (Ol-Sp; °C)		Input *P* (GPa)		$\Delta\log fO_2$ [FMQ]	
			BKN90		B91				Average	*St.* Dev.
			Average	*St.* Dev.	Average	*St.* Dev.	Average	*St.* Dev.		
Greene Point	GP56	Hz	1044	9	926	18	1.1	0.3	−2.87	0.16
Greene Point	GP42	Hz	1030	11	956	5	1.1	0.3	−1.91	0.07
Greene Point	GP38	Lh	1069	7	1041	34	1.1	0.3	−3.05	0.43
Greene Point	GP41	Lh	1009	19	913	6	1.1	0.3	−1.40	0.07
Baker Rocks	BR38	Hz	801	44	849	73	0.8	0.1	0.28	0.31
Baker Rocks	BR42	Hz	940	25	899	21	0.8	0.1	−1.00	0.32
Baker Rocks	BR53	Hz	905	22	884	22	0.8	0.1	−0.48	0.05
Baker Rocks	BR3	Lh	927	27	897	22	0.8	0.1	−1.42	0.22
Baker Rocks	BR29	Lh	990	19	923	14	0.8	0.1	−0.67	0.04
Baker Rocks	BR1	Lh	861	50	844	22	0.8	0.1	−2.06	0.18
Baker Rocks	BR4	Lh	974	33	1020	26	0.8	0.1	−1.32	0.22
Baker Rocks	BR5	Lh	936	20	897	42	0.8	0.1	−1.89	0.57
Baker Rocks	BR55	Lh	952	22	920	41	0.8	0.1	−0.73	0.14
Baker Rocks	BR56	Amp-Lh	990	51	911	19	0.8	0.1	0.30	0.14
Baker Rocks	BR47	Ol-Wb	945	17	884	14	0.8	0.1	−1.14	0.17
Handler Ridge	HR1	Lh	991	46	1061	54	0.9	0.1	0.24	0.17
Handler Ridge	HR2	Lh	1040	52	1072	39	0.9	0.1	0.37	0.10
Handler Ridge	HR3	Lh	833	42	1034	21	0.9	0.1	0.38	0.07
Handler Ridge	HR11	Weh	–	–	1000	37	0.9	0.1	0.61	0.05

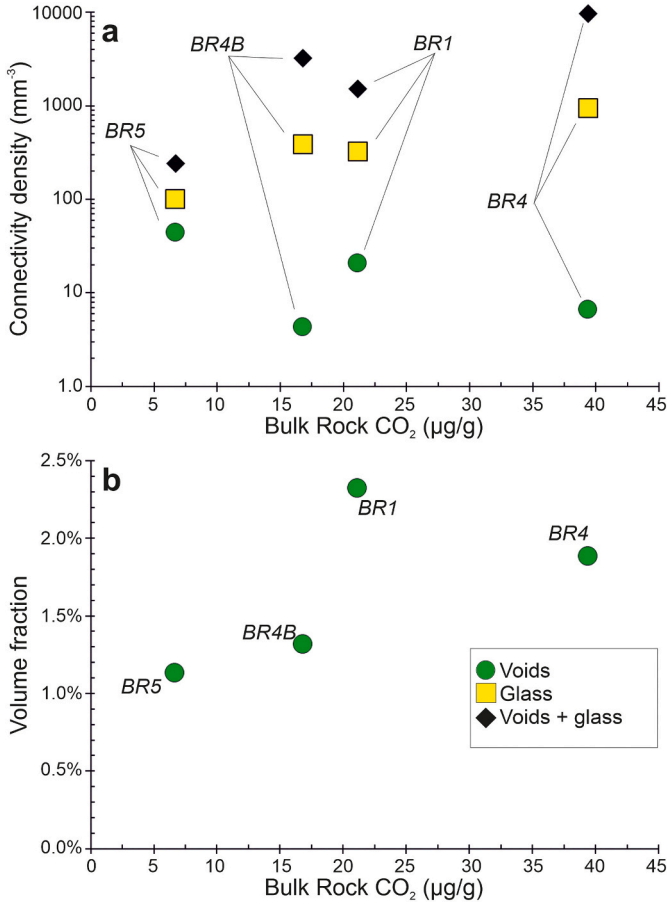

Fig. 8. Comparison between CO_2 released from bulk northern Victoria Land mantle xenoliths and: (a) connectivity density of voids, glass, "voids + glass" phases; (b) volume fraction of voids obtained after 3D reconstruction and segmentation of Volume of Interests.

from Baker Rocks (sample BR38) which record low *T* (800–833 °C), high fO_2 (+0.3 to +0.6 $\Delta\log fO_2$ [FMQ]), but low CO_2 contents (Fig. 7b-c).

7.2.2. CO_2 partitioning and behaviour of fluids in the SCLM

The quantification of the CO_2 stored in the enriched NVL lithospheric mantle has been explored either from the study of nearly un-degassed melt inclusions, representative of primitive, mantle-derived melts (Giacomoni et al., 2020; Oppenheimer et al., 2011), or from the measurement of volatiles in hydrous phases, NAMs and FI in mantle xenoliths (Bonadiman et al., 2009, 2014; Broadley et al., 2016; Correale et al., 2019; Day et al., 2019). Following Giacomoni et al. (2020) and Oppenheimer et al. (2011), the Cenozoic xenoliths-bearing alkali basaltic to basanitic melts at NVL were generated by 3–7% partial melting of an amphibole-bearing peridotite containing 264–418 ppm CO_2. Although the conversion from µg/g to ppm is not recommended, if we assume that the concentration of volatiles per grams of crushed material is representative of the local lithospheric mantle, then it is evident that the measured bulk CO_2 contents (up to 57 µg/g) are not far from the range of values modelled for the NVL mantle from melt inclusions.

Although variable (from 0.1 in olivine from Greene Point up to ~187 µg/g in orthopyroxene from Baker Rocks), the amount of CO_2 stored in the FI seems to be also almost constantly partitioned between the mineral phases inside each xenolith. Indeed, the CO_2 partition between olivine- and orthopyroxene-hosted FI yields values of 0.15–0.33 (0.26 ± 0.09 on average) at Greene Point, 0.03–0.18 (0.10 ± 0.06 on average) at Handler Ridge and 0.04–0.42 (0.22 ± 0.11 on average) at Baker Rocks, irrespective of the lithological variability of the samples (Fig. 6a). Similarly, the CO_2 partitioning between olivine- and clinopyroxene-hosted FI is 0.06–0.18 (0.10 ± 0.05 on average) at Greene Point, 0.01–0.31 (0.12 ± 0.14 on average) at Handler Ridge and 0.10–0.48 (0.27 ± 0.14 on average) at Baker Rocks (Fig. 6b). The partitioning of CO_2 between orthopyroxene and clinopyroxene is quite heterogeneous: Greene Point samples yield constant values (0.31–0.49; 0.42 ± 0.08 on average), while extremely variable ratios typify both Handler Ridge (0.21–4.36; 1.63 ± 1.93 on average) and Baker Rocks (0.80–3.62; 1.73 ± 1.00 on average) xenoliths (Fig. 6c; Table 5). Besides confirming the independency of the *T-P-*fO_2 conditions of the system, these data

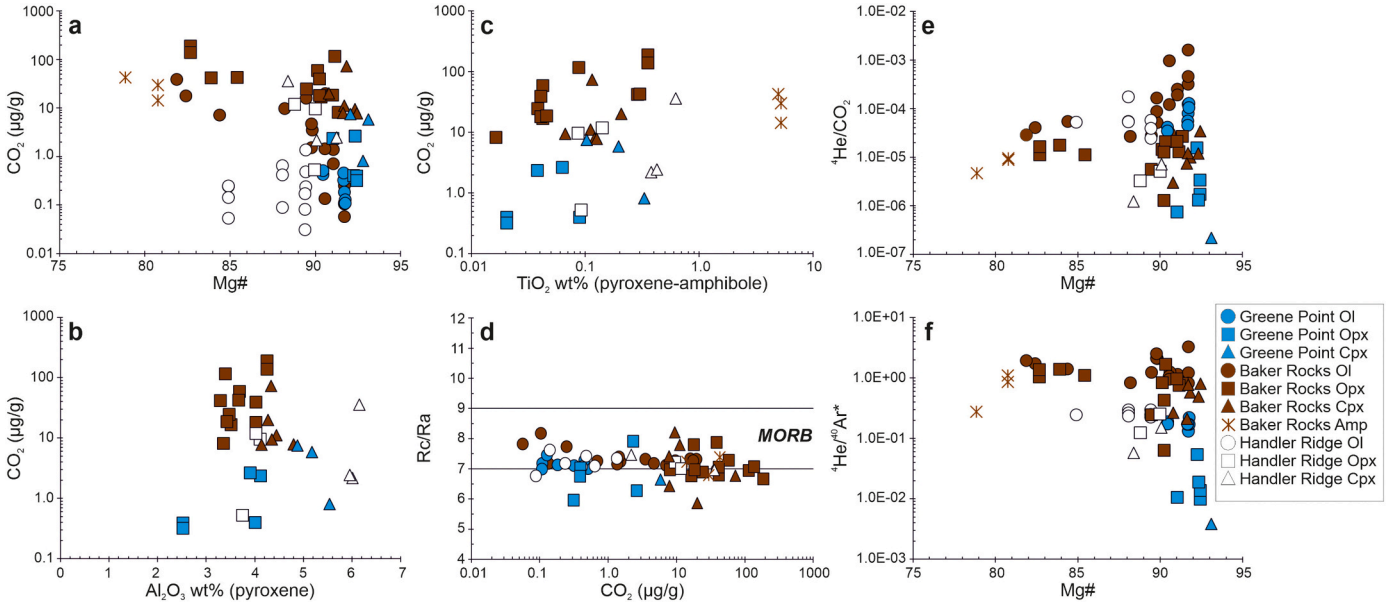

Fig. 9. Comparison between mineral chemistry tracers and CO_2/noble gases absolute concentrations and ratios released by mineral-hosted fluid inclusions in northern Victoria Land ultramafic xenoliths. (a) Mg# versus CO_2 concentration (µg/g). (b) Al_2O_3 (wt%) content of pyroxenes versus CO_2 concentration (µg/g) in fluid inclusions. (c) TiO_2 (wt%) content of pyroxenes and amphibole versus CO_2 concentration (µg/g) in fluid inclusions. (d) CO_2 concentration (µg/g) versus Rc/*Ra* ($^3He/^4He$ corrected for air contamination) in fluid inclusions. (e) Mg# versus $^4He/CO_2$ ratio in fluid inclusions. (f) Mg# versus $^4He/^{40}Ar^*$ ratio in fluid inclusions. In (d), solid lines identify the MORB-like range of $^3He/^4He$ (8 ± 1 Rc/Ra; Graham, 2002).

Table 5
Partitioning of CO_2 (µg/g) between olivine-, orthopyroxene-, and clinopyroxene-hosted fluid inclusions (FI) in ultramafic xenoliths from northern Victoria Land (Antarctica), and $H_2O/(H_2O + CO_2)$ molar ratios calculated for orthopyroxene and clinopyroxene by combining the CO_2 concentration in FI (µg/g) with the H_2O (ppm) retained in the crystal lattices (data from Bonadiman et al., 2009). For each xenolith suite, the average values and standard deviations (*St.* Dev.) on each calculated parameter are also reported. Lh = lherzolite; Hz = harzburgite; Weh = wehrlite; Ol-Wb = olivine-websterite; Amp-Lh = amphibole-bearing lherzolite; Hb = hornblendite; Ol = olivine; Opx = orthopyroxene; Cpx = clinopyroxene.

Locality	Sample	Lithotype	CO_2 partitioning in FI			H_2O (ppm)		$H_2O/(H_2O + CO_2)$ calculated			
			Ol:Opx	Ol:Cpx	Opx:Cpx	Opx	Cpx	Opx Min	Opx Max	Cpx Min	Cpx Max
Greene Point	GP38	Lh	0.37	0.18	0.49	9–16	5–16	0.98	0.99	0.94	0.98
Greene Point	GP41	Lh	0.20	0.06	0.31	9–16	5–16	0.90	0.94	0.62	0.84
Greene Point	GP42	Hz	0.33		–	9–16	–	0.98	0.99	–	–
Greene Point	GP56	Hz	0.15	0.07	0.45	9–16	5–16	0.89	0.94	0.68	0.87
Greene Point	**Average**		**0.26**	**0.10**	**0.42**	–	–	**0.94**	**0.97**	**0.74**	**0.90**
Greene Point	***St.* Dev.**		**0.09**	**0.05**	**0.08**	–	–	**0.04**	**0.03**	**0.14**	**0.06**
Baker Rocks	BR1	Lh	0.27	0.22	0.80	85	382	0.78	0.78	0.93	0.93
Baker Rocks	BR3	Lh	0.21	0.32	1.50	39–166	82–399	0.85	0.96	0.95	0.99
Baker Rocks	BR4	Lh	0.39	0.48	1.21	39–166	82–399	0.80	0.94	0.91	0.98
Baker Rocks	BR5	Lh	0.11	0.39	3.62	39–166	82–399	0.77	0.93	0.96	0.99
Baker Rocks	BR29	Lh	0.13	0.11	0.86	39–166	82–399	0.92	0.98	0.96	0.99
Baker Rocks	BR38	Hz	–	–	–	–	–	–	–	–	–
Baker Rocks	BR42	Hz	0.17	–	–	39–166	–	0.45	0.78	–	–
Baker Rocks	BR47	Ol-Wb	0.04	0.10	2.37	39–166	82–399	0.84	0.96	0.96	0.99
Baker Rocks	BR53 Hz	Hz	0.42	–	–	39–166	–	0.70	0.91	–	–
Baker Rocks	BR53 Hb	Hb	–	–	–	–	–	–	–	–	–
Baker Rocks	BR55 Lh	Lh	0.17	–	–	39–166	–	0.69	0.91	–	–
Baker Rocks	BR55 Hb	Hb	–	–	–	–	–	–	–	–	–
Baker Rocks	BR56	Amp-Lh	0.24	–	–	39–166	–	0.37	0.71	–	–
Baker Rocks	**Average**		**0.22**	**0.27**	**1.73**	–	–	**0.72**	**0.89**	**0.94**	**0.98**
Baker Rocks	***St.* Dev.**		**0.11**	**0.14**	**1.00**	–	–	**0.17**	**0.09**	**0.02**	**0.02**
Handler Ridge	HR1	Lh	0.07	0.31	4.36	–	–	–	–	–	–
Handler Ridge	HR2	Lh	0.03	0.01	0.33	–	–	–	–	–	–
Handler Ridge	HR3	Lh	0.18	0.04	0.21	–	–	–	–	–	–
Handler Ridge	HR11	Weh	–	–		–	–	–	–	–	–
Handler Ridge	**Average**		**0.10**	**0.12**	**1.63**	–	–	–	–	–	–
Handler Ridge	***St.* Dev.**		**0.06**	**0.14**	**1.93**	–	–	–	–	–	–

highlight how the entrapment of CO_2-bearing fluids between olivine and pyroxenes takes place following an almost constant partitioning scheme (Fig. 6a-b). On the other hand, the partitioning of CO_2 between orthopyroxene- and clinopyroxene-hosted FI varies between Greene Point-Handler Ridge, where it is mostly <1, and Baker Rocks samples, where it is close to or larger than unity (Fig. 6c; Table 5).

Theoretical and experimental studies have shown that the CO_2 trapped in mineral-hosted FI represents the dominating species in the

deeply-originated fluid phases infiltrating the SCLM, followed by H_2O (up to 15%), halogens, sulphur species and noble gases (Andersen et al., 1984; Frezzotti and Touret, 2014). With decreasing depth, i.e. moving from the garnet to the spinel field, the composition of the fluid phase in equilibrium with the peridotitic assemblage becomes progressively enriched in CO_2, so that at $P > 2.2$ GPa a phlogopite- and carbonate-bearing garnet peridotite coexists with H_2O-rich fluids, while at $P < 1.7$ GPa an amphibole-bearing spinel peridotite coexists with CO_2-rich fluids (Andersen et al., 1984; Olafsson and Eggler, 1983). In the case of the NVL xenoliths, the absence of carbonates and the shallow *P* recorded by the mineral assemblages (0.7–1.6 GPa; Coltorti et al., 2021) lead to speculate that the most of the CO_2 present in the metasomatizing melt/fluid infiltrating the peridotitic assemblage should have been entrapped in FI. By contrast, H_2O was mostly entrapped in crystal lattices, namely in orthopyroxene (Greene Point = 9–16 ppm H_2O; Baker Rocks = 39–166 ppm H_2O), clinopyroxene (Greene Point = 5–16 ppm H_2O; Baker Rocks = 82–399 ppm H_2O) and amphibole (up to 1.42 wt% H_2O in Baker Rocks xenoliths) (see Bonadiman et al., 2009, 2014). By combining the H_2O content retained in pyroxenes and amphibole with the CO_2 content of the corresponding FI, it is therefore possible to speculate about the $H_2O/(H_2O + CO_2)$ molar ratio of the fluid/melt phases circulating in the Antarctica SCLM. At Greene Point, orthopyroxene yields $H_2O/(H_2O + CO_2)$ between 0.94 ± 0.04 and 0.97 ± 0.03, while clinopyroxene record $H_2O/(H_2O + CO_2)$ from 0.74 ± 0.14 to 0.90 ± 0.06. At Baker Rocks, orthopyroxene yields $H_2O/(H_2O + CO_2)$ from 0.72 ± 0.17 to 0.89 ± 0.09 on average, while clinopyroxene is typified by $H_2O/(H_2O + CO_2)$ molar ratios comprised between 0.94 ± 0.02 and 0.98 ± 0.02 (Table 5). Noteworthy, such results are not far from the maximum $H_2O/(H_2O + CO_2)$ molar ratios (0.86 and 0.88–0.92) measured by Giacomoni et al. (2020) and Oppenheimer et al. (2011) in melt inclusions from NVL, and thought to be representative of the partitioning of volatiles species in the melt/fluid systems at mantle conditions.

Interestingly, the FI hosted in orthopyroxene from the amphibole-bearing peridotites at Baker Rocks are the richest in CO_2, resulting in the lowest $H_2O/(H_2O + CO_2)$ molar ratios (0.59 ± 0.15 to 0.84 ± 0.09 on average by considering amphibole-bearing samples only) (Table 5). Concomitantly, the extreme H_2O contents of amphibole from the same samples (8400–14,200 ppm), although accompanied by significant amounts of CO_2 in FI, drive the $H_2O/(H_2O + CO_2)$ molar ratios in amphibole to values >0.99. This decoupling confirms that the partitioning of H_2O and CO_2 between the fluid phase and peridotitic system during metasomatic processes is intimately connected to the stability of hydrous phases (Andersen et al., 1984; Olafsson and Eggler, 1983; Wyllie, 1978). From another perspective, this can also indicate that the H_2O/CO_2 ratios of the melts produced during partial melting of a metasomatized mantle can change as a function of the eutectic melting proportions of the mineral phases (see Casetta et al., 2020).

7.3. Origin of CO_2 and geodynamic implications

The strict relationships between the CO_2 budget stored in the FI and the fertility/depletion of their host minerals confirms what was reported for other mantle xenolith suites from diverse tectonic settings, such as Central Mexico, Wilcza Góra and West Eifel (Central Europe) (Rizzo et al., 2018, 2021; Sandoval-Velasquez et al., 2021). However, the absolute CO_2 amounts released by FI in pyroxenes from the Antarctica mantle xenoliths, and especially from Baker Rocks ones, are generally higher than those from Central Europe (West Eifel: orthopyroxene = 0–22 μg/g, clinopyroxene = 1–59 μg/g; Wilcza Góra: orthopyroxene = 25–107 μg/g, clinopyroxene = 19–20 μg/g; Rizzo et al., 2018, 2021) and Central Mexico (orthopyroxene = 0–5 μg/g, clinopyroxene = 0–14 μg/g; Sandoval-Velasquez et al., 2021). Different is the case of olivine, that in Central Mexico and West Eifel rocks is extremely gas-depleted (always <1 μg/g CO_2), while in Wilcza Góra peridotites contains significant amounts of CO_2 (4–66 μg/g) (Rizzo et al., 2018), even higher than those of Baker Rocks. Such results suggest that relatively shallow SCLM portions beneath intra-continental rift systems, usually affected by complex metasomatic episodes, can store the highest contents of CO_2 in their FI.

By coupling the concentration of CO_2 in FI with mineral chemistry and 3D textural characterization of mantle xenoliths from NVL, some information about the origin of fluids and their relationships with the melts circulating in the SCLM during the Jurassic to Cenozoic metasomatic/refertilization events can be extracted. The $^3He/^4He$ ratio corrected for air contamination (Rc/*Ra*) measured on the same FI (Correale et al., 2019) does not show any significant correlation with CO_2, lying at almost constant Rc/*Ra* of 7.1 ± 0.4 (Fig. 9d). This highlights how the $^3He/^4He$ ratio of the Antarctic SCLM bears witness of a pervasive and long-lasting recycling of volatiles, being not affected by the degree of depletion or enrichment of the local mantle domains (Broadley et al., 2016; Correale et al., 2019; Day et al., 2019). By contrast, the storage and mobility of CO_2 in the lithospheric mantle is more sensitive to the infiltration of metasomatic/refertilization agents. Ultramafic xenoliths from NVL bear witness of a complex history of events that occurred in the Antarctica SCLM, starting from depletion episode(s) taking place with variable extent between the Archean and the Cenozoic, mostly in the spinel stability field (Melchiorre et al., 2011; Perinelli et al., 2006). The information provided by the distribution of CO_2 in FI well fits such an evolutive scenario. Indeed, relicts of a deeper (P = 0.8–1.6 GPa), more depleted and possibly older (*Re*—Os ages on sulphides always >565 *Ma*; Melchiorre et al., 2011) mantle are preserved at Greene Point. Here, harzburgites and lherzolites constituted by high-Mg# mineral phases, low absolute CO_2 concentrations in FI, coupled with low $^4He/CO_2$ and $^4He/^{40}Ar^*$ occur (Fig. 9e-f). The slight increase of CO_2 concentrations, $^4He/CO_2$ and $^4He/^{40}Ar^*$ ratios in the Greene Point and some of the Baker Rocks samples at almost constant Mg# could be consistent with the onset of the tholeiitic refertilization episode related to the development of the Jurassic Ferrar large magmatic event that superimposed on the depleted domains, locally being responsible for the genesis of the low-Mg# (83–85) lherzolites-harzburgites (e.g., matrixes of composite samples BR53-BR55) (Fig. 9a; see also Pelorosso et al., 2016). The extreme CO_2 enrichment of the Baker Rocks mantle xenoliths has then to be ascribed to the Cenozoic mobilization of alkaline, volatile-rich melts/fluids, which permeated the mantle domains beneath this area, causing both cryptic, modal and stealth metasomatism (Coltorti et al., 2004, 2021), as testified by the noble gases/CO_2 ratios in the range of typical mantle production ratios and magmatic fluids. The younger age of the metasomatism at Baker Rocks is also supported by *Re*—Os ages on sulphides from the amphibole-bearing sample BR56, mostly lying between 145 and 46 *Ma* (Melchiorre et al., 2011). From such a sequence of events, some speculations on the behaviour and amount of CO_2 retained in the various metasomatic/refertilizing agents can be made:

- The CO_2-depleted nature of the Greene Points rocks is mainly related to the melt extraction episodes experienced by this portion of SCLM. The tholeiitic refertilization related to the onset of the Jurassic Ferrar magmatism affected the Greene Point mantle heterogeneously (Coltorti et al., 2021; Pelorosso et al., 2016), and took place without inducing a CO_2-enrichment. This was probably due to the low budget of volatiles dissolved in the SiO_2-saturated melts that infiltrated the mantle and/or the position of Greene Point, lying at the very edge of the area affected by the emplacement of Ferrar magmas (Fig. 1).
- A massive mobilization of CO_2 temporally and spatially associated to the alkaline metasomatism took place at Baker Rocks shortly before the effective infiltration of the consanguineous melts, from which amphibole formed (Fig. 9; Coltorti et al., 2004, 2021). This is evident from: i) the selective enrichment of CO_2 in primary orthopyroxene with respect to secondary formed (metasomatic) phases, such as clinopyroxene, amphibole and olivine, in amphibole-bearing xenoliths (Fig. 9); ii) the high CO_2 concentrations measured in pyroxenes (higher in orthopyroxene than clinopyroxene) from anhydrous

lherzolites, which are comparable to those reported from pyroxenes in the amphibole-bearing rocks (Fig. 9). If we suppose that the CO_2-enrichment was only concomitant with the infiltration of alkaline melts, then we should expect to detect it limited to amphibole-bearing rocks, and with CO_2 partitioning favouring clinopyroxene over orthopyroxene, but this is not the case (Figs. 6 and 9). By contrast, if we hypothesize that the FI originated by melt-free fluxing postdating the alkaline metasomatism, then it should be expected that the addition of CO_2 should have induced a decrease of the H_2O activity in the ambient fluid and the destabilization of amphibole and/or orthopyroxene (Aulbach et al., 2020; Wyllie, 1978).

- Further evidence for the differential timing of infiltration of fluid and melt comes from the distribution of FI in the Baker Rocks composite samples. Here, the absence of FI trails propagating through both the matrix and the hornblenditic veins confirms that the infiltration of fluids occurred before or during the (melt-related) formation of amphibole veins. Moreover, most of the FI trails in the lherzolitic/harzburgitic matrices are cut by the hornblenditic veins, while some others are associated with the inter-granular reaction zones at the edges between matrix and veins (Fig. 2). This indicates that the majority of the FI were entrapped by the SCLM prior to the arrival of the melt, while others formed by volatiles exsolution from the incoming melt. This scenario is somehow consistent with what was observed for mantle xenoliths from Tenerife (Canary Islands). Here, the FI entrapped in peridotites at *P* of 0.7–1.7 GPa were originated by exsolution from a volatile-rich, alkaline carbonatitic melt prior/during its infiltration in the upper mantle (Frezzotti et al., 2002). Afterwards, the evolution of this metasomatic agent was driven by its position: inter-granular melt reacted with pyroxenes, unmixing into a carbonaceous silicate melt and a CO_2-rich fluid, while intra-granular, FI-hosted fluid separated into two fluids (pure CO_2 and a H_2O-NaCl brine) (Frezzotti et al., 2002).
- The onset of CO_2 fluxing in the SCLM beneath Antarctica before the arrival of the alkaline metasomatic melt is also consistent with the mantle outgassing models proposed in the literature to explain the mobilization of fluids and trace elements in the deep mantle (Andersen et al., 1984; Frezzotti and Touret, 2014). In this framework, the most plausible hypothesis is that fluids associated with the alkaline magmatism infiltrated the Antarctica SCLM shortly before to the rising of the consanguineous melts. This scenario resulted in the ascent of alkaline melts with progressively decreasing volatile content, lately grading into volatile-poorer magmas, which induced the formation of both anhydrous and hydrous cumulates at Browning Pass and Mt. Overlord (Coltorti et al., 2021; Perinelli et al., 2017).
- Martin et al. (2015) suggested that xenoliths from neighbouring SCLM portions (i.e. southern Victoria Land) bear witness of the infiltration of small amounts (<0.1 vol%) of carbonatitic melts. However, the only evidence for carbonatitic magmatism in this area is dated back to the Cambrian (526–536 *Ma*; Hall et al., 1995), therefore it is highly unlikely that the NVL mantle could have been able to preserve this kind of modification only in the FI (not in mineral phases), and through such a long and articulated geodynamic evolution. Although high, the amount of CO_2 stored in northern Victoria Land mantle xenoliths cannot be related to the infiltration of a carbonatitic agent, being more plausibly representative of independent CO_2 fluxing (Andersen et al., 1984; Frezzotti and Touret, 2014) or exsolution of a fluid phase from a CO_2-rich alkaline silicate melt (Scambelluri et al., 2009). This confirms what was already recognized by Perinelli et al. (1998), who suggested that the inter-granular glass inclusions in some Baker Rocks and Greene Point samples are associated with the infiltration of CO_2-bearing melt in the Antarctica SCLM. This scenario is also consistent with the model proposed by Broadley et al. (2016) and Panter et al. (2018), who hypothesized that subduction-related CO_2-bearing agents recycled in the asthenosphere during the protracted Ross subduction were re-mobilized before/during the metasomatic event that produced the amphibole-bearing veins in the Antarctica SCLM and then the Cenozoic alkaline magmatism.

8. Conclusions

Besides confirming the important role played by fluids stored in both intra- and inter-granular domains in mantle peridotites (Créon et al., 2017; Frezzotti and Touret, 2014), our study enabled, for the first time, to quantify the distribution of CO_2 through different domains of the SCLM, and link it to the articulated geodynamic evolution of the region.

The main results of our study are summarized as follows:

1. In the NVL ultramafic xenoliths, the distribution of CO_2 in FI varies from 0 to 39 μg/g in olivine up to 187 μg/g in orthopyroxene, for corresponding bulk CO_2 contents between 0 and 11 μg/g (Handler Ridge and Greene Point) and 2–57 μg/g (Baker Rocks).
2. The systematic relationships between bulk CO_2 contents, volume and connectivity density of voids and glasses can be used to quantify the amount of fluids and melts originally preserved in a relatively fertile mantle and eventually understand the role played by decompression-induced cracking in mantle xenoliths in affecting the melt/fluid phases. The original Antarctica SCLM may have retained ~1.1 vol% fluid and ~ 0.2 vol% melt phases, and the CO_2 storage occurred mainly in FI trails inside mineral phases. In some samples, the excess of CO_2 released by bulk xenoliths with respect to single phases indicates that between 10 and 80% of CO_2 can also be efficiently stored in inter-granular fluids, which represent an important reservoir of carbon in the SCLM.
3. The relationships between CO_2, noble gases in FI, mineral chemistry (Mg#, TiO_2, Al_2O_3) and *T-P-fO2* conditions recorded by the xenoliths highlighted that the CO_2 budget stored in FI is not related to a simple "layering" of the lithospheric mantle, to the onset of degassing processes and/or to the entrapment depth, being instead strictly related to the composition of the host minerals, and thus to the nature of the eventual metasomatic agent/s that infiltrated the Antarctic SCLM.
4. The bulk CO_2 contents hosted in the FI (up to 57 μg/g) are not far from the range of values modelled for the NVL mantle from melt inclusions (264–418 ppm; Giacomoni et al., 2020). Irrespective of the lithological variability of the samples, the amount of CO_2 is constantly partitioned between olivine- and orthopyroxene-hosted FI (from 0.10 ± 0.06 to 0.26 ± 0.09) as well as between olivine- and clinopyroxene-hosted FI (from 0.10 ± 0.05 to 0.27 ± 0.14).
5. The $H_2O/(H_2O + CO_2)$ molar ratios calculated by comparing the CO_2 contents of the FI to the H_2O amounts retained in the lattices of orthopyroxene and clinopyroxene (Bonadiman et al., 2009, 2014) vary between 0.72 ± 0.17 and 0.97 ± 0.03, being not far from the values assumed as representative of the partition of volatiles in the melt/fluid systems at mantle conditions (0.86–0.92; Giacomoni et al., 2020; Oppenheimer et al., 2011). The variation in $H_2O/(H_2O + CO_2)$ molar ratios in orthopyroxene between amphibole-free and amphibole-bearing samples confirms that the partitioning of H_2O and CO_2 between the fluid phase and peridotitic system during metasomatic processes is intimately connected to the stability of hydrous phases (Andersen et al., 1984; Olafsson and Eggler, 1983; Wyllie, 1978). In turn, this means that a peridotitic system in which equilibrium conditions are not achieved (open system) is able to produce magmas with variable H_2O/CO_2 ratios as a function of the eutectic melting proportions of the mineral phases (Casetta et al., 2020).
6. When coupled with detailed petrological investigations, the distribution of CO_2 and noble gases in FI is a useful tool for reconstructing the geodynamic evolution of specific SCLM portions. Relicts of a deeper, more depleted and older mantle are preserved at Greene Point, where high-Mg# harzburgites and lherzolites have low absolute CO_2 concentrations in the FI, coupled with low $^4He/CO_2$ and $^4He/^{40}Ar^*$. The slight increase in CO_2, $^4He/CO_2$ and $^4He/^{40}Ar^*$ in

Greene Point and some of the Baker Rocks samples, concomitant with the genesis of low-Mg# (83–85) lherzolites-harzburgites is ascribed to the onset of the tholeiitic refertilization associated with the Jurassic tholeiitic magmatism. The extreme enrichment in CO_2 of Baker Rocks mantle xenoliths is induced by the more recent mobilization of alkaline, volatiles-rich metasomatic agents.

7. The entrapment of CO_2-rich fluids occurred shortly before the infiltration of the associated alkaline melts, which induced the formation of amphibole (Coltorti et al., 2004, 2021). The CO_2 mobilized during this metasomatic event probably originated from recycling of CO_2-bearing components in the asthenosphere during the protracted Ross subduction (Broadley et al., 2016; Giacomoni et al., 2020; Panter et al., 2018).

Funding

This work was supported by the funding provided by Elettra Synchrotron Radiation Facility (Trieste, Italy) to [MC] for the project 20160125 "Volumetric estimation of intergranular melts and textural reconstruction of mantle xenoliths" at the SYRMEP beamline, as well as by the Italian National Research Program Grants (PRIN) 2017 Projects 20178LPCPW to [MC] and 2017LMNLAW to [ALR].

Author contributions statement

FC: sample preparation, minerals handpicking, conceptualization, investigation, data evaluation and modelling, writing and supervision; ALR: minerals handpicking, fluid inclusions analyses, data evaluation and interpretation, writing and reviewing; BF and LF: evaluation and interpretation of petrography and mineral chemistry data, writing and reviewing; TN and RA: mineral chemistry analyses, evaluation and interpretation of petrography and mineral chemistry data, reviewing and editing; GL and LM: Synchrotron X-Ray computed microtomography analyses, 3D processing and data evaluation, reviewing and editing; PPG: sample collection, field work, assistance in Synchrotron X-Ray computed microtomography analyses; MC: sample collection, field work, project supervision and conceptualization, data evaluation and modelling, writing and editing.

Declaration of Competing Interest

The authors declare that they have no known competing financial interests or personal relationships that could have appeared to influence the work reported in this paper.

Acknowledgments

Authors are grateful to Michel Grégoire and an anonymous reviewer for their constructive comments on an earlier version of the manuscript, as well as to Michael Roden for his careful editorial handling. We thank INGV-Palermo for allowing the access to the facilities of the noble gas isotope laboratory. We are grateful to Mariagrazia Misseri and Mariano Tantillo for helping in sample preparation and analysis of fluid inclusions. We also thank the SYRMEP team for the technical support during beamtime.

Appendix A. Supplementary data

Supplementary data to this article can be found online at https://doi.org/10.1016/j.lithos.2022.106643.

References

Aiuppa, A., Casetta, F., Coltorti, M., Stagno, V., Tamburello, G., 2021. Carbon concentration increases with depth of melting in Earth's upper mantle. Nat. Geosci. 14 (9), 697–703. https://doi.org/10.1038/s41561-021-00797-y.

Andersen, T., Neumann, E.R., 2001. Fluid inclusions in mantle xenoliths. Lithos 55 (1–4), 301–320. https://doi.org/10.1016/S0024-4937(00)00049-9.

Andersen, T., O'Reilly, S.Y., Griffin, W.L., 1984. The trapped fluid phase in upper mantle xenoliths from Victoria, Australia: implications for mantle metasomatism. Contrib. Mineral. Petrol. 88 (1–2), 72–85.

Anderson, K.R., Poland, M.P., 2017. Abundant carbon in the mantle beneath Hawai'i. Nat. Geosci. 10 (9), 704–708. https://doi.org/10.1038/ngeo3007.

Arai, S., 1994. Characterization of spinel peridotites by olivine-spinel compositional relationships: review and interpretation. Chem. Geol. 113, 191–204. https://doi.org/10.1016/0009-2541(94)90066-3.

Aulbach, S., Lin, A.B., Weiss, Y., Yaxley, G.M., 2020. Wehrlites from continental mantle monitor the passage and degassing of carbonated melts. Geochem. Perspect. Lett. 15, 30–34.

Ballhaus, C., Berry, R.F., Green, D.H., 1991. High pressure experimental calibration of the olivine-orthopyroxene-spinel oxygen geobarometer: implications for the oxidation state of the upper mantle. Contrib. Mineral. Petrol. 107, 27–40. https://doi.org/10.1007/BF00311183.

Bonadiman, C., Hao, Y., Coltorti, M., Dallai, L., Faccini, B., Huang, Y., Xia, Q., 2009. Water contents of pyroxenes in intraplate lithospheric mantle. Eur. J. Mineral. 21 (3), 637–647. https://doi.org/10.1127/0935-1221/2009/0021-1935.

Bonadiman, C., Nazzareni, S., Coltorti, M., Comodi, P., Giuli, G., Faccini, B., 2014. Crystal chemistry of amphiboles: implications for oxygen fugacity and water activity in lithospheric mantle beneath Victoria Land, Antarctica. Contrib. Mineral. Petrol. 167 (3), 984. https://doi.org/10.1007/s00410-014-0984-8.

Boudoire, G., Rizzo, A.L., Di Muro, A., Grassa, F., Liuzzo, M., 2018. Extensive CO_2 degassing in the upper mantle beneath oceanic basaltic volcanoes: first insights from Piton de la Fournaise volcano (La Réunion Island). Geochim. Cosmochim. Acta 235, 376–401. https://doi.org/10.1016/j.gca.2018.06.004.

Brett, R.C., Russell, J.K., Andrews, G.D.M., Jones, T.J., 2015. The ascent of kimberlite: Insights from olivine. Earth Planet. Sci. Lett. 424, 119–131. https://doi.org/10.1016/j.epsl.2015.05.024.

Brey, G.P., Kohler, T., 1990. Geothermobarometry in Four-phase Lherzolites II. New Thermobarometers, and Practical Assessment of existing Thermobarometers. J. Petrol. 31, 1353–1378. https://doi.org/10.1093/petrology/31.6.1353.

Broadley, M.W., Ballentine, C.J., Chavrit, D., Dallai, L., Burgess, R., 2016. Sedimentary halogens and noble gases within Western Antarctic xenoliths: Implications of extensive volatile recycling to the sub continental lithospheric mantle. Geochim. Cosmochim. Acta 176, 139–156. https://doi.org/10.1016/j.gca.2015.12.013.

Canil, D., 1990. Experimental study bearing on the absence of carbonate in mantle-derived xenoliths. Geology 18 (10), 1011–1013. https://doi.org/10.1130/0091-7613(1990)018<1011:ESBOTA>2.3.CO;2.

Casetta, F., Giacomoni, P.P., Ferlito, C., Bonadiman, C., Coltorti, M., 2020. The evolution of the mantle source beneath Mt. Etna (Sicily, Italy): from the 600 ka tholeiites to the recent trachybasaltic magmas. Int. Geol. Rev. 62 (3), 338–359. https://doi.org/10.1080/00206814.2019.1610979.

Casetta, F., Ickert, R.B., Mark, D.F., Giacomoni, P.P., Bonadiman, C., Ntaflos, T., Zanetti, A., Coltorti, M., 2021. The Variscan subduction inheritance in the Southern Alps Sub-Continental Lithospheric Mantle: Clues from the Middle Triassic shoshonitic magmatism of the Dolomites (NE Italy). Lithos 380, 105856. https://doi.org/10.1016/j.lithos.2020.105856.

Coltorti, M., Beccaluva, L., Bonadiman, C., Salvini, L., Siena, F., 2000. Glasses in mantle xenoliths as geochemical indicators of metasomatic agents. Earth Planet. Sci. Lett. 183 (1–2), 303–320. https://doi.org/10.1016/S0012-821X(00)00274-0.

Coltorti, M., Beccaluva, L., Bonadiman, C., Faccini, B., Ntaflos, T., Siena, F., 2004. Amphibole genesis via metasomatic reaction with clinopyroxene in mantle xenoliths from Victoria Land, Antarctica. Lithos 75 (1–2), 115–139. https://doi.org/10.1016/j.lithos.2003.12.021.

Coltorti, M., Bonadiman, C., Casetta, F., Faccini, B., Giacomoni, P.P., Pelorosso, B., Perinelli, C., 2021. Nature and evolution of the northern Victoria Land Lithospheric Mantle (Antarctica) as revealed by ultramafic xenoliths. Geol. Soc. Lond. Mem. 56 https://doi.org/10.1144/M56-2020-11. M56-2020–11.

Condamine, P., Médard, E., 2014. Experimental melting of phlogopite-bearing mantle at 1 GPa: Implications for potassic magmatism. Earth Planet. Sci. Lett. 397, 80–92. https://doi.org/10.1016/j.epsl.2014.04.027.

Correale, A., Pelorosso, B., Rizzo, A.L., Coltorti, M., Italiano, F., Bonadiman, C., Giacomoni, P.P., 2019. The nature of the West Antarctic Rift System as revealed by noble gases in mantle minerals. Chem. Geol. 524, 104–118. https://doi.org/10.1016/j.chemgeo.2019.06.020.

Cottrell, E., Kelley, K.A., Hauri, E.H., Le Voyer, M., 2019. Mantle carbon contents for mid-ocean ridge segments. Interdisc. Earth Data Alliance. https://doi.org/10.1594/IEDA/111333.

Créon, L., Rouchon, V., Youssef, S., Rosenberg, E., Delpech, G., Szabo, C., Guyot, F., 2017. Highly CO_2-supersaturated melts in the Pannonian lithospheric mantle–a transient carbon reservoir? Lithos 286, 519–533. https://doi.org/10.1016/j.lithos.2016.12.009.

Dasgupta, R., 2013. Ingassing, storage, and outgassing of terrestrial carbon through geologic time. Rev. Mineral. Geochem. 75 (1), 183–229. https://doi.org/10.2138/rmg.2013.75.7.

Dasgupta, R., Hirschmann, M.M., 2006. Melting in the Earth's deep upper mantle caused by carbon dioxide. Nature 440 (7084), 659–662. https://doi.org/10.1038/nature04612.

Dasgupta, R., Hirschmann, M.M., 2010. The deep carbon cycle and melting in Earth's interior. Earth Planet. Sci. Lett. 298 (1–2), 1–13. https://doi.org/10.1016/j.epsl.2010.06.039.

Dasgupta, R., Hirschmann, M.M., Smith, N.D., 2007. Partial melting experiments of peridotite+ CO_2 at 3 GPa and genesis of alkalic ocean island basalts. J. Petrol. 48 (11), 2093–2124. https://doi.org/10.1093/petrology/egm053.

Day, J.M., Harvey, R.P., Hilton, D.R., 2019. Melt-modified lithosphere beneath Ross Island and its role in the tectono-magmatic evolution of the West Antarctic Rift System. Chem. Geol. 518, 45–54. https://doi.org/10.1016/j.chemgeo.2019.04.012.

Dick, H.J.B., Bullen, T., 1984. Chromian spinel as a petrogenetic indicator in abyssal and alpine-type peridotites and spatially associated lavas. Contrib. Mineral. Petrol. 86, 54–76. https://doi.org/10.1007/BF00373711.

Eggler, D.H., 1976. Does CO_2 cause partial melting in the low-velocity layer of the mantle? Geology 4 (2), 69–72. https://doi.org/10.1130/0091-7613(1976)4<69:DCCPMI>2.0.CO;2.

Elliot, D.H., Fleming, T.H., 2018. The Ferrar large Igneous Province: field and geochemical constraints on supra-crustal (high-level) emplacement of the magmatic system. Geol. Soc. Lond., Spec. Publ. 463 (1), 41–58. https://doi.org/10.1144/SP463.1.

Faccini, B., Rizzo, A.L., Bonadiman, C., Ntaflos, T., Seghedi, I., Grégoire, M., Coltorti, M., 2020. Subduction-related melt refertilisation and alkaline metasomatism in the Eastern Transylvanian Basin lithospheric mantle: evidence from mineral chemistry and noble gases in fluid inclusions. Lithos 364, 105516. https://doi.org/10.1016/j.lithos.2020.105516.

Farsang, S., Louvel, M., Zhao, C., Mezouar, M., Rosa, A.D., Widmer, R.N., Redfern, S.A., 2021. Deep carbon cycle constrained by carbonate solubility. Nature. Communications 12 (1), 1–9. https://doi.org/10.1038/s41467-021-24533-7.

Foley, S., 1991. High-pressure stability of the fluor-and hydroxy-endmembers of pargasite and K-richterite. Geochim. Cosmochim. Acta 55 (9), 2689–2694. https://doi.org/10.1016/0016-7037(91)90386-J.

Foley, S.F., Fischer, T.P., 2017. An essential role for continental rifts and lithosphere in the deep carbon cycle. Nat. Geosci. 10 (12), 897–902. https://doi.org/10.1038/s41561-017-0002-7.

Franz, L., Wirth, R., 1997. Thin intergranular melt films and melt pockets in spinel peridotite xenoliths from the Rhön area (Germany): early stage of melt generation by grain boundary melting. Contrib. Mineral. Petrol. 129 (4), 268–283.

Frezzotti, M.L., Touret, J.L., 2014. CO_2, carbonate-rich melts, and brines in the mantle. Geosci. Front. 5 (5), 697–710. https://doi.org/10.1016/j.gsf.2014.03.014.

Frezzotti, M.L., Andersen, T., Neumann, E.R., Simonsen, S.L., 2002. Carbonatite melt–CO_2 fluid inclusions in mantle xenoliths from Tenerife, Canary Islands: a story of trapping, immiscibility and fluid–rock interaction in the upper mantle. Lithos 64 (3–4), 77–96. https://doi.org/10.1016/S0024-4937(02)00178-0.

Frezzotti, M.L., Ferrando, S., Peccerillo, A., Petrelli, M., Tecce, F., Perucchi, A., 2010. Chlorine-rich metasomatic H_2O–CO_2 fluids in amphibole-bearing peridotites from Injibara (Lake Tana region, Ethiopian plateau): nature and evolution of volatiles in the mantle of a region of continental flood basalts. Geochim. Cosmochim. Acta 74 (10), 3023–3039. https://doi.org/10.1016/j.gca.2010.02.007.

Galvez, M.E., Pubellier, M., 2019. How do subduction zones regulate the carbon cycle?. In: Deep Carbon: Past to Present. Cambridge University Press, pp. 276–312. https://doi.org/10.3929/ethz-b-000389115.

Giacomoni, P.P., Bonadiman, C., Casetta, F., Faccini, B., Ferlito, C., Ottolini, L., Coltorti, M., 2020. Long-term storage of subduction-related volatiles in Northern Victoria Land lithospheric mantle: Insight from olivine-hosted melt inclusions from McMurdo basic lavas (Antarctica). Lithos 378, 105826. https://doi.org/10.1016/j.lithos.2020.105826.

Graham, D.W., 2002. Noble gas isotope geochemistry of Mid-Ocean Ridge and Ocean Island Basalts: characterization of mantle source reservoirs. Rev. Mineral. Geochem. 47, 247–317. https://doi.org/10.2138/rmg.2002.47.8.

Hall, C.E., Cooper, A.F., Parkinson, D.L., 1995. Early Cambrian carbonatite in Antarctica. J. Geol. Soc. 152 (4), 721–728. https://doi.org/10.1144/gsjgs.152.4.0721.

Hauri, E.H., Maclennan, J., McKenzie, D., Gronvold, K., Oskarsson, N., Shimizu, N., 2018. CO_2 content beneath northern Iceland and the variability of mantle carbon. Geology 46 (1), 55–58. https://doi.org/10.1130/G39413.1.

Hazen, R.M., Schiffries, C.M., 2013. Why deep carbon? Rev. Mineral. Geochem. 75 (1), 1–6. https://doi.org/10.2138/rmg.2013.75.1.

Hirschmann, M.M., 2018. Comparative deep Earth volatile cycles: the case for C recycling from exosphere/mantle fractionation of major (H_2O, C, N) volatiles and from H_2O/Ce, CO_2/Ba, and CO_2/Nb exosphere ratios. Earth Planet. Sci. Lett. 502, 262–273. https://doi.org/10.1016/j.epsl.2018.08.023.

Howell, D., Stachel, T., Stern, R.A., Pearson, D.G., Nestola, F., Hardman, M.F., Navon, O., 2020. Deep carbon through time: Earth's diamond record and its implications for carbon cycling and fluid speciation in the mantle. Geochim. Cosmochim. Acta 275, 99–122. https://doi.org/10.1016/j.gca.2020.02.011.

Kleinschmidt, G., Tessensohn, F., Vetter, U., 1987. Paleozoic Accretion at the Paleopacific margin of Antarctica. Polarforschung 57 (1/2), 1–8.

Klügel, A., 1998. Reactions between mantle xenoliths and host magma beneath La Palma (Canary Islands): constraints on magma ascent rates and crustal reservoirs. Contrib. Mineral. Petrol. 131 (2), 237–257. https://doi.org/10.1007/s004100050391.

Lanzafame, G., Casetta, F., Giacomoni, P.P., Donato, S., Mancini, L., Coltorti, M., Ferlito, C., 2020. The Skaros effusive sequence at Santorini (Greece): petrological and geochemical constraints on an interplinian cycle. Lithos 362, 105504. https://doi.org/10.1016/j.lithos.2020.105504.

Le Voyer, M., Kelley, K.A., Cottrell, E., Hauri, E.H., 2017. Heterogeneity in mantle carbon content from CO_2-undersaturated basalts. Nature. Communications 8 (1), 1–8. https://doi.org/10.1038/ncomms14062.

Malusà, M.G., Frezzotti, M.L., Ferrando, S., Brandmayr, E., Romanelli, F., Panza, G.F., 2018. Active carbon sequestration in the Alpine mantle wedge and implications for long-term climate trends. Sci. Rep. 8 (1), 1–8. https://doi.org/10.1038/s41598-018-22877-7.

Martin, A.P., Price, R.C., Cooper, A.F., McCammon, C.A., 2015. Petrogenesis of the rifted southern Victoria Land lithospheric mantle, Antarctica, inferred from petrography, geochemistry, thermobarometry and oxybarometry of peridotite and pyroxenite xenoliths from the Mount Morning eruptive Centre. J. Petrol. 56 (1), 193–226. https://doi.org/10.1093/petrology/egu075.

Marty, B., 2012. The origins and concentrations of water, carbon, nitrogen and noble gases on Earth. Earth Planet. Sci. Lett. 313, 56–66. https://doi.org/10.1016/j.epsl.2011.10.040.

Maire, E., Withers, P.J., 2014. Quantitative X-ray tomography. International Materials Reviews 59, 1–43.

Melchiorre, M., Coltorti, M., Bonadiman, C., Faccini, B., O'Reilly, S.Y., Pearson, N.J., 2011. The role of eclogite in the rift-related metasomatism and Cenozoic magmatism of Northern Victoria Land, Antarctica. Lithos 124 (3–4), 319–330. https://doi.org/10.1016/j.lithos.2010.11.012.

Melchiorre, M., Faccini, B., Grégoire, M., Benoit, M., Casetta, F., Coltorti, M., 2020. Melting and metasomatism/refertilisation processes in the Patagonian sub-continental lithospheric mantle: a review. Lithos 354, 105324. https://doi.org/10.1016/j.lithos.2019.105324.

Miller, W.G.R., Holland, T.J.B., Gibson, S.A., 2016. Garnet and spinel oxybarometers: new internally consistent multi-equilibria models with applications to the oxidation state of the lithospheric mantle. J. Petrol. 57, 1199–1222. https://doi.org/10.1093/petrology/egw037.

Muirhead, J.D., Fischer, T.P., Oliva, S.J., Laizer, A., van Wijk, J., Currie, C.A., Ebinger, C. J., 2020. Displaced cratonic mantle concentrates deep carbon during continental rifting. Nature 582 (7810), 67–72. https://doi.org/10.1038/s41586-020-2328-3.

Mukasa, S.B., Dalziel, I.W., 2000. Marie Byrd Land, West Antarctica: Evolution of Gondwana's Pacific margin constrained by zircon U-Pb geochronology and feldspar common-Pb isotopic compositions. Geol. Soc. Am. Bull. 112 (4), 611–627. https://doi.org/10.1130/0016-7606(2000)112<611:MBLWAE>2.0.CO;2.

Olafsson, M., Eggler, D.H., 1983. Phase relations of amphibole, amphibole-carbonate, and phlogopite-carbonate peridotite: petrologic constraints on the asthenosphere. Earth Planet. Sci. Lett. 64 (2), 305–315. https://doi.org/10.1016/0012-821X(83)90212-1.

Oppenheimer, C., Moretti, R., Kyle, P.R., Eschenbacher, A., Lowenstern, J.B., Hervig, R. L., Dunbar, N.W., 2011. Mantle to surface degassing of alkalic magmas at Erebus volcano, Antarctica. Earth Planet. Sci. Lett. 306 (3–4), 261–271. https://doi.org/10.1016/j.epsl.2011.04.005.

O'Reilly, S.Y., Griffin, W.L., 2013. Mantle metasomatism. In: Metasomatism and the Chemical Transformation of Rock. Springer, Berlin, Heidelberg, pp. 471–533. https://doi.org/10.1007/978-3-642-28394-9_12.

Panter, K.S., Castillo, P., Krans, S., Deering, C., McIntosh, W., Valley, J.W., Blusztajn, J., 2018. Melt origin across a rifted continental margin: a case for subduction-related metasomatic agents in the lithospheric source of alkaline basalt, NW Ross Sea, Antarctica. J. Petrol. 59 (3), 517–558. https://doi.org/10.1093/petrology/egy036.

Pearce, J.A., Barker, P.F., Edwards, S.J., Parkinson, I.J., Leat, P.T., 2000. Geochemistry and tectonic significance of peridotites from the South Sandwich arc-basin system. South Atlantic. Contrib. Mineral. Petrol. 139, 36–53. https://doi.org/10.1007/s004100050572.

Pelorosso, B., Bonadiman, C., Coltorti, M., Faccini, B., Melchiorre, M., Ntaflos, T., Gregoire, M., 2016. Pervasive, tholeiitic refertilisation and heterogeneous metasomatism in Northern Victoria Land lithospheric mantle (Antarctica). Lithos 248, 493–505. https://doi.org/10.1016/j.lithos.2016.01.032.

Pelorosso, B., Bonadiman, C., Coltorti, M., Melchiorre, M., Giacomoni, P.P., Ntaflos, T., Gregoire, M., Benoit, M., 2017. Role of percolating melts in Antarctic subcontinental lithospheric mantle: New insights from Handler Ridge mantle xenoliths (northern Victoria Land, Antarctica). In: Special Paper of the Geological Society of America, pp. 133–150. https://doi.org/10.1130/2017.2526(07).

Perinelli, C., Armienti, P., Trigila, R., Aurisicchio, C., 1998. Intergranular melt inclusions within ultramafic xenoliths from Baker Rocks and Greene Point volcanics (Northern Victoria Land, Antarctica). Terra Antarct. 5 (2), 217–233.

Perinelli, C., Armienti, P., Dallai, L., 2006. Geochemical and O-isotope constraints on the evolution of lithospheric mantle in the Ross Sea rift area (Antarctica). Contrib. Mineral. Petrol. 151 (3), 245–266. https://doi.org/10.1007/s00410-006-0065-8.

Perinelli, C., Gaeta, M., Armienti, P., 2017. Cumulate xenoliths from Mt. Overlord, northern Victoria Land, Antarctica: a window into high pressure storage and differentiation of mantle-derived basalts. Lithos 268, 225–239. https://doi.org/10.1016/j.lithos.2016.10.027.

Pilet, S., 2015. Generation of low-silica alkaline lavas: Petrological constraints, models, and thermal implications. The interdisciplinary Earth: a volume in Honor of Don L. Anderson. Geol. Soc. Am. Spec. Pap. 514, 281–304. https://doi.org/10.1130/2015.2514(17).

Plank, T., Manning, C.E., 2019. Subducting carbon. Nature 574 (7778), 343–352. https://doi.org/10.1038/s41586-019-1643-z.

Polacci, M., Mancini, L., Baker, D.R., 2010. The contribution of synchrotron X-ray computed microtomography to understanding volcanic processes. J. Synchrotron Radiat. 17, 215–221. https://doi.org/10.1107/S0909049509048225.

Pouchou, J.L., Pichoir, F., 1991. Quantitative analysis of homogeneous or stratified microvolumes applying the model "PAP". In: Electron Probe Quantitation. Springer, Boston, MA, pp. 31–75. https://doi.org/10.1007/978-1-4899-2617-3_4.

Rizzo, A.L., Pelorosso, B., Coltorti, M., Ntaflos, T., Bonadiman, C., Matusiak-Małek, M., Bergonzoni, G., 2018. Geochemistry of noble gases and CO_2 in fluid inclusions from lithospheric mantle beneath Wilcza Góra (lower Silesia, Southwest Poland). Frontiers. Earth Sci. 6, 215. https://doi.org/10.3389/feart.2018.00215.

Rizzo, A.L., Faccini, B., Casetta, F., Faccincani, L., Ntaflos, T., Italiano, F., Coltorti, M., 2021. Melting and metasomatism in West Eifel and Siebengebirge Sub-Continental Lithospheric Mantle: evidence from concentrations of volatiles in fluid inclusions

and petrology of ultramafic xenoliths. Chem. Geol. 120400 https://doi.org/10.1016/j.chemgeo.2021.120400.
Roedder, E., 1965. Liquid CO_2 inclusions in olivine-bearing nodules and phenocrysts from basalts. Am. Mineral. 50 (10), 1746–1782.
Roedder, E., 1984. Fluid inclusions. Rev. Mineral. 12.
Rosenthal, A., Hauri, E.H., Hirschmann, M.M., 2015. Experimental determination of C, F, and H partitioning between mantle minerals and carbonated basalt, CO_2/Ba and CO_2/Nb systematics of partial melting, and the CO_2 contents of basaltic source regions. Earth Planet. Sci. Lett. 412, 77–87. https://doi.org/10.1016/j.epsl.2014.11.044.
Saal, A.E., Hauri, E.H., Langmuir, C.H., Perfit, M.R., 2002. Vapour undersaturation in primitive mid-ocean-ridge basalt and the volatile content of Earth's upper mantle. Nature 419 (6906), 451–455. https://doi.org/10.1038/nature01073.
Sandoval-Velasquez, A., Rizzo, A.L., Frezzotti, M.L., Saucedo, R., Aiuppa, A., 2021. The composition of fluids stored in the central Mexican lithospheric mantle: Inferences from noble gases and CO_2 in mantle xenoliths. Chem. Geol. 576, 120270 https://doi.org/10.1016/j.chemgeo.2021.120270.
Scambelluri, M., Vannucci, R., De Stefano, A., Preite-Martinez, M., Rivalenti, G., 2009. CO_2 fluid and silicate glass as monitors of alkali basalt/peridotite interaction in the mantle wedge beneath Gobernador Gregores, Southern Patagonia. Lithos 107 (1–2), 121–133. https://doi.org/10.1016/j.lithos.2008.06.015.
Shirey, S., Smit, K., Pearson, D., Walter, M., Aulbach, S., Brenker, F., Weiss, Y., 2019. Diamonds and the mantle geodynamics of carbon. Deep Carbon. In: Past to Present, pp. 89–128. https://doi.org/10.1017/9781108677950.005.
Stachel, T., Harris, J.W., 2009. Formation of diamond in the Earth's mantle. J. Phys. Condens. Matter 21 (36), 364206. https://doi.org/10.1088/0953-8984/21/36/364206.
Suarez, C.A., Edmonds, M., Jones, A.P., 2019. Earth Catastrophes and their Impact on the Carbon Cycle. Elements 15, 301–306. https://doi.org/10.2138/gselements.15.5.301.
Taylor, W.R., Green, D.H., 1988. Measurement of reduced peridotite-COH solidus and implications for redox melting of the mantle. Nature 332 (6162), 349–352. https://doi.org/10.1038/332349a0.
Thompson, A.B., 1992. Water in the Earth's upper mantle. Nature 358 (6384), 295–302. https://doi.org/10.1038/358295a0.
Tumiati, S., Fumagalli, P., Tiraboschi, C., Poli, S., 2013. An experimental study on COH-bearing peridotite up to 3.2 GPa and implications for crust–mantle recycling. J. Petrol. 54 (3), 453–479. https://doi.org/10.1093/petrology/egs074.
Wallace, M., Green, D.H., 1991. The effect of bulk rock composition on the stability of amphibole in the upper mantle: implications for solidus positions and mantle metasomatism. Mineral. Petrol. 44 (1–2), 1–19.
Wyllie, P.J., 1977. Effects of H_2O and CO_2 on magma generation in the crust and mantle. J. Geol. Soc. 134 (2), 215–234. https://doi.org/10.1144/gsjgs.134.2.0215.
Wyllie, P.J., 1978. Mantle fluid compositions buffered in peridotite-CO_2-H_2O by carbonates, amphibole, and phlogopite. J. Geol. 86 (6), 687–713. https://doi.org/10.1086/649737.
Zhu, W., Gaetani, G.A., Fusseis, F., Montési, L.G., De Carlo, F., 2011. Microtomography of partially molten rocks: three-dimensional melt distribution in mantle peridotite. Science 332 (6025), 88–91. https://doi.org/10.1126/science.1202221.